Myc Dysregulation in Activated Macrophages Initiates Iron-Mediated Lipid Peroxidation that Fuels Type I Interferon and Compromises TB Resistance

Running title:

Myc dysregulation fuels pathological macrophage activation

Shivraj M. Yabaji[1]

Vadim Zhernovkov[2]

Prasanna Babu Araveti[1]

Suruchi Lata[1]

Oleksii S. Rukhlenko[2]

Salam Al Abdullatif[3]

Yuriy Alekseev[5]

Qicheng Ma[12]

Gargi Dayama[12]

Nelson C. Lau[1,12]

William R. Bishai[4]

Nicholas A. Crossland[1,5]

Joshua D. Campbell[3]

Boris N. Kholodenko[2,6,7]

Alexander A. Gimelbrant[8]

Lester Kobzik[9]

Igor Kramnik[1,10,11,13, 14]

1. The National Emerging Infectious Diseases Laboratory, Boston University, Boston, MA

2. Systems Biology Ireland, School of Medicine, University College Dublin, Dublin 4, Ireland

3. Department of Medicine, Boston University Chobanian & Avedisian School of Medicine, Boston, MA

4. Center for TB Research, Johns Hopkins School of Medicine, Baltimore, Maryland

5. The Department of Pathology and Laboratory Medicine, Boston University Chobanian & Avedisian School of Medicine, Boston, MA 02118.

6. Conway Institute of Biomolecular & Biomedical Research, University College Dublin, Dublin 4, Ireland

7. Department of Pharmacology, Yale University School of Medicine, New Haven CT, USA

8. Altius Institute for Biomedical Sciences, Seattle, WA, USA

9. Cellecta, Inc., Mountain View, CA

10. Pulmonary Center, The Department of Medicine, Boston University Chobanian & Avedisian School of Medicine.

11. Dept. of Microbiology, Boston University Chobanian & Avedisian School of Medicine

12. Department of Biochemistry, and Cell Biology and Genome Science Institute, Boston University Chobanian & Avedisian School of Medicine

13. Lead contact

14. Corresponding author (ikramnik@bu.edu)

Igor Kramnik, MD, PhD Boston University School of Medicine, NEIDL

620 Albany St., Boston, MA 02118, phone: (617) 358-9187, e-mail: ikramnik@bu.edu

Abstract.

A quarter of human population is infected with *Mycobacterium tuberculosis*, but less than 10% of those infected develop clinical, mostly pulmonary, TB. To dissect mechanisms of susceptibility in immunocompetent individuals, we developed a genetically defined *sst1*-susceptible mouse model that uniquely reproduces a defining feature of human TB: development of necrotic lung lesions after infection with virulent Mtb. In this study, we explored the connectivity of the *sst1*-regulated pathways during prolonged macrophage activation with TNF. We determined that the aberrant response of the *sst1*-susceptible macrophages to TNF was primarily driven by conflicting Myc and antioxidant response pathways that resulted in a coordinated failure to properly sequester intracellular iron and activate ferroptosis inhibitor enzymes. Consequently, iron-mediated lipid peroxidation fueled IFNβ superinduction and sustained the Type I Interferon (IFN-I) pathway hyperactivity that locked the *sst1*-susceptible macrophages in a state of unresolving stress and compromised their resistance to Mtb. The accumulation of the aberrantly activated, stressed, macrophages within granuloma microenvironment led to the local failure of anti-tuberculosis immunity and tissue necrosis. Our findings suggest a novel link between metabolic dysregulation in macrophages and susceptibility to TB, offering insights into potential therapeutic targets aimed at modulating macrophage function and improving TB control.

Introduction.

Thousands of years of co-evolution with modern humans has made *Mycobacterium tuberculosis* (Mtb) arguably the most successful human pathogen(*1*). It currently colonizes approximately a quarter of the global population(*2*). Most Mtb-infected people develop latent TB, in which the host responses either eliminate or sequester the bacteria inside a granuloma structure (*3, 4*). However, about 5-10% of Mtb-infected individuals will eventually develop active TB either within a year after the primary infection, or later in their life after re-activation of persistent bacteria or re-infection(*5-8*). A plethora of genetic, developmental and environmental factors contribute to TB progression in individuals that initially resisted the pathogen(*9, 10*).

A major unanswered question in TB pathogenesis, is the mechanism of lung tissue damage and subsequent development of cavities in immunocompetent hosts. Infection of the lung is central to TB's evolutionary success because it allows the pathogen to spread among human hosts via aerosols. After systemic dissemination from primary lesions, Mtb can be found in many human organs(*11, 12*). However, approximately 85% of the disease develops in the lungs(*4*). Necrotic lesions are the major pathologic manifestation of pulmonary TB ranging from central necrosis in organized granulomas during primary TB to massive necrotizing pneumonia and the formation of cavities in post-primary pulmonary TB. In humans, both types of necrotic lung lesions develop in immunocompetent hosts despite the presence of active T cell mediated immune response.

Existing mechanistic concepts explaining the lesion necrosis fall into two main categories: i) *inadequate* local immunity that allows exuberant bacterial replication and

production of virulence factors that drive tissue necrosis, vs. ii) *excessive* effector immunity that results in immune-mediated tissue damage (*13-15*). Although both scenarios are credible, they are mechanistically distinct and would require different therapeutic strategies. Therefore, in-depth understanding of mechanisms of pulmonary TB progression in immunocompetent hosts is necessary for accurate patient stratification and for the development of personalized approaches to immune modulation(*16*).

Mouse models have been successfully used for mechanistic studies of Mtb infection, although classical inbred mouse strains routinely used in TB research, such as C57BL/6 (B6) and BALB/c, do not develop human-like necrotic TB lesions(*17*). Nevertheless, even in these models, Mtb predominantly replicates in the lungs irrespective of the route of infection(*18*). Mouse models that recapitulate the necrotization of pulmonary TB lesions have also been developed (reviewed in (*19*). We have previously found that C3HeB/FeJ mice develop necrotizing granulomas after infection with virulent Mtb and mapped several genetic loci of TB susceptibility using a cross of the C3HeB/FeJ with the resistant B6 mice (*20-22*). We found a single locus on chromosome 1, *sst1* (***s***uper***s***usceptibility to ***t***uberculosis 1), was responsible for the control of the necrotization of TB lesions (*23*). The *sst1*-susceptible mice develop necrotic lung lesions irrespective of the route of infection – aerosol, intravenous or intradermal(*20, 21, 24-26*) – thus demonstrating a common underlying mechanism.

We further found that the *sst1* locus primarily controls macrophage-mediated resistance to intracellular pathogens (*24, 27-29*) , associated with hyperactivity of the type I interferon (IFN-I) pathway in vitro and in vivo (*29-31*). Of note, the hyperactivity of

IFN-I pathway has been associated with TB susceptibility and the disease progression in human patients and experimental models (*13, 32-34*). However, mechanisms that regulate the IFN-I hyperactivity and their roles in susceptibility to TB were insufficiently elucidated. The *sst1*-mediated susceptibility recapitulates the morphologic and mechanistic hallmarks of human TB disease and provides a model to study both the upstream mechanisms responsible for the IFN-I pathway hyperactivity(*30*) and its downstream consequences(*35*).

The *sst1* locus encodes the SP110 (*24*) and SP140 (*36*) proteins – known as interferon inducible chromatin binding proteins(*37*). The expression of mRNAs encoding both proteins is greatly diminished in mice that carry the *sst1* susceptibility allele and protein expression is undetectable for both(*30, 36*). Both proteins were shown to be involved in regulation of type I interferon pathway(*36, 38*). The overexpression of SP110b in macrophages increases their resistance to intracellular bacteria in vitro(*24*). However, the Sp140 gene knockout mice were extremely susceptible to several intracellular bacteria including virulent Mtb(*36*). It was suggested that SP140 plays a major role in TB susceptibility, possibly via epistatic interactions. Better understanding the roles of SP110 and SP140 proteins in specific biochemical pathways is necessary to link them to TB pathogenesis.

Recent progress in understanding the SP140-mediated mechanisms was boosted by the discovery that its hypomorphic alleles were associated with susceptibility to chronic inflammatory diseases - multiple sclerosis and Crohn's disease(*39, 40*). SP140 mutations in a cohort of Crohn's disease patients predicted responsiveness to anti-TNF therapy, suggesting their roles in driving the aberrant TNF response in

humans. Mechanistically, SP140 was implicated in silencing “lineage-inappropriate” and developmental genes and maintenance of heterochromatin in activated macrophages (*40*). It regulated macrophage fate and transcriptional activity by binding to and inhibiting topoisomerases(*41*). Understanding how these molecular mechanisms contribute to the control of macrophage activation during chronic inflammation of various etiologies would allow for their optimal therapeutic modulation.

Previously, we found that prolonged TNF stimulation of B6.Sst1S macrophages in vitro uniquely induced an aberrant response that was characterized by the IFNβ superinduction, a coordinated upregulation of interferon-stimulated genes (ISGs), and markers of proteotoxic stress (PS) and the integrated stress response (ISR). While the initial responses of the B6 and B6.Sst1S macrophages to TNF were similar, the expression of the aberrant response markers in TNF-stimulated B6.Sst1S macrophages occurred in a step wise manner starting 8 – 12 h after continuous TNF stimulation. The PS and IFNβ superinduction were the earliest events followed by ISR. The ISR induction, but not that of the PS, was prevented by the type I IFN receptor blockade, whereas the inhibitors of stress kinase JNK prevented the IFNβ superinduction. The upregulation of all of these pathways was prevented by a reactive oxygen scavenger (BHA) (*30*). These data suggested that oxidative stress was driving the aberrant activation of the *sst1*-susceptible macrophages, although its root cause(s) remained unknown.

Current literature provides ample evidence of the crosstalk between the above pathways: 1) stress kinase activation by oxidative stress(*42, 43*); 2) promotion of type I interferon (IFN-I) responses by stress kinases(*44-46*); 3) suppression of AOD by IFN-I

(*47, 48*); 4) suppression of IFN responses and AOD by Myc (*49-51*). However, complex interactions and regulatory dependencies of these pathways remain poorly understood, especially in the contexts of specialized non-transformed cells, such as activated macrophages (F**ig.1A**).

In this study, we specifically addressed how a single genetic locus, *sst1*, regulated these pathways' connectivity and hierarchy in primary TNF-activated macrophages, a cell state relevant to TB granuloma microenvironment(*52*). We determined that the aberrant response of the *sst1*-susceptible macrophages to TNF was primarily driven by conflicting Myc and anti-oxidant response pathways. Their dysregulation in activated macrophages resulted in a failure to sequester intracellular iron, the accumulation of oxidative stress products, sustained activity of stress-activated kinase JNK and, eventually, the IFNβ superinduction. This cascade of coincident pathways locked the *sst1*-susceptible macrophages in a state of persistent unresolving stress fueled by Myc and sustained by IFN-I and lipid peroxidation. The accumulation of the aberrantly activated macrophages within granuloma microenvironment led to the local failure of anti-tuberculosis immunity and tissue necrosis.

.

Results.

1. The *sst1* locus controls diverse trajectories of macrophage activation by TNF

To explore the spectrum of TNF responses in the B6 and B6.Sst1S BMDMs, we compared gene expression in the BMDM populations either naïve, or after 24 h of stimulation with TNF (10 ng/ml) using single-cell RNA sequencing (scRNA-seq)(**Fig.1B**). The naïve macrophage populations of both backgrounds were similar. All BMDMs responded to TNF stimulation, as evidenced by the de novo formation of clusters 1- 6, where cluster 3 appeared exclusively in the resistant (B6) and clusters 4 and 5 in the susceptible (B6.Sst1S) macrophage populations (**Fig.1C** and **Suppl.Fig.1A**). After TNF stimulation, the expression of the *sst1*-encoded Sp110 and Sp140 genes coordinately increased only in the B6 macrophages (**Fig.1D** and **Suppl.Fig.1B**). The entire IFN pathway was dramatically upregulated in TNF stimulated B6.Sst1S cells that lacked the Sp110 and Sp140 expression, but it was upregulated to a lesser degree in cluster 3 exclusive for TNF-stimulated Sp110/140-positive B6 macrophages (**FIG.1E** and **Suppl.Fig.1C**).

To determine the relatedness of the diverse macrophage subpopulations, as they emerge during TNF stimulation, we performed trajectory analysis that clearly demonstrated partial overlap and the divergence between the trajectories of TNF-stimulated resistant (RT) and susceptible (ST) subpopulations (**Fig.1F**). Subpopulations sp1 and sp2 of the B6 and B6.Sst1S macrophages were closely related and were characterized by the upregulation of cell division pathways in both backgrounds (**Fig.1G**). Cell cycle analysis demonstrated that TNF stimulation increased the fraction of macrophages in S phase (**Suppl.Table 1**).

The susceptible (ST) and resistant(RT) activation trajectories diverged as the RT transitioned from sp2 to sp3, but the ST transitioned from sp2 to sp4 and 5. The transition from sp2 to sp3 in the resistant B6 BMDMs, was characterized by an increase of the G1/S ratio, the downregulation of anabolic pathways involved in cell growth and replication (E2F and Myc), and the upregulation of anti-oxidant genes (**Fig.1G and 1H**). In contrast, in the susceptible B6.Sst1S macrophages, the sp2 transitioned to subpopulations sp4 and sp5 that were characterized by the decreased G1/S ratios as compared to sp3, signifying an increased G1 – S transition (**Suppl. Table 2**). The sp4 represented an intermediate state between sp2 and sp5 and was primarily characterized by the upregulation of the IFN pathway (**Fig.1G**), as evidenced by the upregulation of known IFN-I pathway activation markers (Rsad2, IL1rn, Cxcl10) (**Suppl.Fig.1C and D**). Of note, IFN-I pathway genes were upregulated in all TNF-stimulated B6.Sst1S macrophages in agreement with the paracrine effect of IFNβ, whose increased production by TNF-stimulated B6.Sst1S macrophages we have described previously (*30*).

In contrast, ST macrophages in sp5 uniquely demonstrated a coordinated upregulation of the IFN, TGFb, Myc, E2F, and stress response (p53 and UPR) pathways (**Fig.1G**). They upregulated the Integrated Stress Response (ISR) genes (Ddit3/Chop10, Atf3, Ddit4, Trib1, Trib3, Chac1) in parallel with markers of immune suppression and apoptosis (Cd274/PD-L1, Fas, Trail/Tnfsf10, Id2, and a pro-apoptotic ligand – receptor pair Tnfsf12/Tweak and Tnfrsf12a/Tweak receptor) (**Suppl.Fig.1D**). Interestingly, the expression of Irf7 and several IFN-inducible genes, such as B2m,

Cxcl10, and Ube2l6 was reduced in the sp5 cells, suggesting partial dampening of their IFN-I responsiveness (**Suppl.Fig.1C**).

Taken together, the single cell trajectory analysis revealed that sp5 represented a terminal state of the aberrant B6.Sst1S macrophage activation by TNF that was characterized the coordinated upregulation of stress, pro-apoptotic and immunosuppression genes. Unexpectedly, the stress escalation coincided with paradoxical activity of Myc and E2F pathways. Transition to this state in the susceptible macrophage population was preceded by IFN-I pathway upregulation (sp2 – sp4). In contrast, the sp2 – sp3 transition in the wild type macrophages was coincident with upregulation of both the Sp110 and Sp140 genes and was accompanied by the termination of cell cycle and the upregulation of antioxidant defense pathways. Therefore, we concluded that in resistant TNF-stimulated macrophages the *sst1* locus-encoded genes promoted the activation of the AOD pathway either directly, or by suppressing the IFN-I pathway.

To begin exploring the hierarchy and crosstalk of these pathways, we used an unbiased computational approach to define the Sp110 and Sp140 regulatory networks. First, we inferred a mouse macrophage gene regulatory network using the GENIE3 algorithm (*53*) and external gene expression data for mouse macrophages derived from Gene Expression Omnibus (GEO) (*54*). This network represents co-expression dependencies between transcription factors and their potential target genes, calculated based on mutual variation in expression level of gene pairs (*55, 56*). This analysis revealed that in mouse macrophages the Sp110 and Sp140 genes co-expressed with targets of Nfe2l1/2 (Nuclear Factor Erythroid 2 Like 1/2) and Mtf (metal-responsive

transcription factor) TFs that are involved in regulating macrophage responses to oxidative stress and heavy metals, respectively (**Fig.1I**). Taken together, our experimental data and the unbiased network analysis suggested that in TNF-stimulated macrophages the *sst1*-encoded Sp110 and/or Sp140 gene(s) might be primarily involved in regulating AOD.

2. Dysregulated AOD activation in B6.Sst1S macrophages

Next, we compared the expression of upstream regulators of AOD in B6 and B6.Sst1S macrophages during TNF activation. Our previous studies demonstrated that the earliest differences between the B6 and B6.Sst1S BMDMs occurred between 8 and 12 h of TNF stimulation, concomitant with the upregulation of the SP110 protein in the B6 macrophages and heat shock proteins in the mutant cells(*30*). Comparing the time course of major transcriptional regulators of AOD in TNF-stimulated B6 and B6.Sst1S macrophages during this critical time interval, we observed higher upregulation of NRF2 protein in TNF stimulated B6 BMDMs (**Fig.2A**). The NRF1 levels were not substantially upregulated after TNF stimulation and were similar in B6 and B6.Sst1S BMDMs (**Fig.2A** and **Suppl.Fig.2A**).

The NRF2 difference was observed both in cytoplasmic and nuclear fractions (**Fig.2B** and **C**, respectively). The levels of NRF2 negative regulators Keap1 and β-TrCP (**Fig.2A**), and Bach1 (**Fig.2B** and **C**) were similar in both backgrounds and did not notably change after TNF stimulation. Quantitative microscopy confirmed that at 12 h of TNF stimulation the cytoplasmic and nuclear NRF2 levels significantly increased in B6 but not in B6.Sst1S BMDMs (**Fig.2D**, **E** and **Suppl.Fig.2B**). In contrast, the levels of

Nrf2 mRNA induced by TNF were higher in the mutant macrophages suggesting post transcriptional regulation(**Fig.2F**). Therefore, we measured the rates of NRF2 protein degradation 6 – 8 h after TNF stimulation but found no difference (**Fig.2H** and **2I**).

Using EMSA, we demonstrated that binding activity of nuclear NRF2 to its target DNA at 8 and 12 h after TNF stimulation was greater in the resistant B6 BMDMs (**Fig.2G**). To identify core pathways controlled by the *sst1* locus during this critical period, we compared global mRNA expression profiles of the B6 and B6.Sst1S macrophages after 12 h of TNF stimulation using RNA-seq. This analysis confirmed that the Sp110 and Sp140 genes were strongly upregulated by TNF stimulation exclusively in the B6 macrophages. Gene set enrichment analysis (GSEA) of genes differentially expressed between TNF-stimulated B6.Sst1S and B6 macrophages at this critical junction revealed that the IFN response, Myc, E2F target gene, Hypoxia, UV response and DNA repair pathways were upregulated in the mutant macrophages, while the detoxification of reactive oxygen species, cholesterol homeostasis, fatty acid metabolism and oxidative phosphorylation, peroxisome and lysosome pathways were downregulated (**Suppl.Table 3**). Functional pathway profiling using KEGG and Reactome databases also highlighted the upregulation of genes involved in oxidative stress and cellular senescence in mutant macrophages. In contrast, the wild type macrophages upregulated genes involved in detoxification of reactive oxygen species, inhibition of ferroptosis and peroxisome function (**Suppl.Table 4**). Supporting these findings, the total antioxidant capacity of the B6 macrophages after TNF stimulation increased to significantly higher levels, as compared to the B6.Sst1S (**Suppl.Fig.2C**).

Transcription factor binding site analysis of genes specifically upregulated by TNF in B6, but not B6.Sst1S, macrophages (B6-specific cluster) revealed an enrichment of Nfe2l1/Nfe2l2, Bach1 and Mafk sequence motifs, i.e. binding sites of transcription factors regulating AOD. In contrast, overrepresentation of E2F, Egr1 and Pbx3 transcription factor binding sites was found for genes in the Sst1S-specific cluster (**Suppl.Table 5**). A master regulator analysis using Virtual Inference of Protein Activity by Enriched Regulon Analysis (VIPER) algorithm also revealed a key role for Nfe2l (NF-E2-like) transcription factors (TFs) as regulators of genes differentially induced by TNF in B6 and B6.Sst1S BMDMs (**Suppl. Table 6**).

To further investigate this inference, we analyzed the expression of a gene ontology set “response to oxidative stress” (GO0006979, 416 genes) and observed clear separation of these genes in two clusters in an *sst1*-dependent manner (**Fig.2J** and **2K**). This analysis demonstrated that the response to oxidative stress in the *sst1* mutant macrophages was dysregulated, but not paralyzed. For example, the upregulation of well-known NRF2 target genes Heme oxygenase 1 (Hmox1) and (NAD(P)H quinone dehydrogenase 1 (Nqo1) were similar in B6 and B6.Sst1S BMDMs (**Suppl.Fig.2D** and **2E**, respectively).

A subset of antioxidant defense genes whose expression was concordant with Sp110 and Sp140 in B6 macrophages represented genes that are known to be involved in iron storage (ferritin light and heavy chains, Ftl and Fth), ROS detoxification and maintenance of redox state (Cat, G6pdx, Gstm1, Gpx4, Prdx6, Srxn1, Txn2 and Txnrd1) **(Fig.2J)**. We hypothesized that their coordinate downregulation in TNF-stimulated

B6.Sst1S macrophages sensitized the mutant cells to iron-mediated oxidative damage and played a pivotal role in shaping their divergent activation trajectory.

3. Persistent TNF stimulation of B6.Sst1S macrophages leads to increased accumulation of lipid peroxidation products and IFN-I pathway hyperactivity.

To test this hypothesis, first we explored the intracellular iron storage. Both the ferritin light (Ftl) and heavy (Fth) chain genes were dysregulated in TNF-stimulated B6.Sst1S BMDMs. While the Fth mRNA was upregulated by TNF in B6 BMDMs, it remained at a basal level in the B6.Sst1S cells (**Fig.3A**). The Ftl mRNA level was significantly reduced after TNF stimulation in B6.Sst1S macrophages but remained at the basal level in B6 (**Fig.3B**). Accordingly, the expression of FTL protein was reduced in B6.Sst1S BMDMs after 12 h of TNF stimulation, and both FTL and FTH proteins were reduced at 24 h (**Fig.3C**). In parallel, the levels of GPX1 and GPX4 proteins were also substantially reduced by 24 h (**Fig.3D**). The glutathione peroxidase 4 (GPX4) protein plays a central role in preventing ferroptosis because of its unique ability to reduce hydroperoxide in complex membrane phospholipids and, thus, limit self-catalytic lipid peroxidation (*57*). Thus, the reduced intracellular iron storage capacity in TNF-stimulated B6.Sst1S BMDMs was followed by the decline of the major lipid peroxidation inhibitor GPX4. Accordingly, we observed increases in an intracellular labile iron pool (LIP, **Fig.3E**), an intracellular accumulation of oxidized lipids (**Fig.3F),** a toxic terminal lipid peroxidation (LPO) products malondialdehyde (MDA, **Fig.3G**) and 4-hydroxynonenal (4-HNE, **Fig.3H**). Treatment with the LPO inhibitor Ferrostatin-1 (Fer1)

and blockade of type I interferon receptor (IFNAR1) prevented the 4-HNE accumulation (**Fig.3I**-**J,** and **Suppl.Fig.3A**-**B**).

After 48h of TNF stimulation the levels of the labile iron pool (LIP) and LPO remained significantly elevated in B6.Sst1S macrophages (**Suppl.Fig.3C – G**). By then, we noted moderate cell death in their cultures (**Fig.3K**) that further increased by 72h. Treatments with Fer1, the antioxidant butylated hydroxyanisole (BHA), or IFNAR1 blockade each prevented the cell death. (**Fig.3L**). These data demonstrated that during prolonged TNF stimulation, B6.Sst1S macrophages incur iron-mediated oxidative damage that may lead to cell death via IFN-mediated lipid peroxidation.

Next, we wanted to test whether the IFN-I pathway hyperactivity in TNF stimulated B6.Sst1S macrophages was responsible for the initial dysregulation of the Ftl, Fth and AOD gene expression, i.e. at 8 – 12 h of TNF stimulation. IFNAR1 blockade, however, did not increase either the NRF2 and FTL protein levels, or the Fth, Ftl and Gpx1 mRNA levels above those treated with isotype control antibodies(**Fig.4A – C**). The mRNA expression of the interferon-inducible gene Rsad2, however, was suppressed, demonstrating the efficiency of the IFNAR1 blockade (**Fig.4D**). Of note, the IFNAR1 blockade did not prevent the Ifnβ mRNA superinduction (**Fig.4E**), thus rejecting another hypothesis that the Ifnβ superinduction in B6.Sst1S macrophages was driven via an IFNβ – IFNAR1 positive feedback. In contrast, treatment of B6.Sst1S macrophages with Fer-1 or the iron chelator DFO during initial TNF stimulation inhibited both the Ifnβ and Rsad2 mRNAs upregulation (**Fig.4F** and **Suppl. Fig.3H,** respectively). Importantly, Fer-1 treatment also reduced the Ifnβ and Rsad2 levels in B6.Sst1S macrophages when added at 18 h after TNF stimulation, i.e. during

established aberrant response (**Fig. 4G** and **Suppl. Fig.3I**). Thus, lipid peroxidation was involved in both the initiation and maintenance of the IFNβ superinduction and IFN-I pathway hyperactivity driven by TNF. Also, the activity of JNK stress kinase was upregulated in B6.Sst1S macrophages, as compared to B6, after 12 h of TNF stimulation, i.e. during the aberrant activation stage confirming persistent stress (**Fig.4H** and **I).**

The *sst1*-encoded Sp110 and Sp140 genes were described as interferon-induced genes, and SP140 protein was implicated in maintenance of heterochromatin silencing in activated macrophages (*37, 40*). Therefore, we hypothesized that their deficiency in the TNF-stimulated B6.Sst1S mutants may lead to the upregulation of silenced transposons and, thus, trigger the IFNβ upregulation via intracellular RNA sensors, i.e. by an autonomous mechanism unrelated to the AOD dysregulation. We examined the transcriptomes of B6 and B6.Sst1S macrophages before and after TNF stimulation for the presence of persistent viruses or transposons using a custom bioinformatics pipeline (*58*). No exogenous mouse viral RNAs were detected. A select set of mouse LTR-containing endogenous retroviruses (ERV's) (*59*), and non-retroviral LINE L1 elements were expressed at a basal level before and after TNF stimulation, but their levels in the B6.Sst1S BMDMs were similar to or lower than those seen in B6 (**Suppl.Fig.4A-C**). We also tested the accumulation of dsRNA using deep sequencing of macrophage small RNAs and failed to detect evidence of transposon-derived dsRNAs (**Suppl.Fig.4D**). We concluded from these findings that the majority of the basal transposon RNAs in macrophages exist primarily as single-stranded mRNAs that evade triggering interferon pathway. The above analyses allowed us to exclude the

overexpression of persistent viral or transposon RNAs as a primary mechanism of the IFN-I pathway hyperactivity.

The above experiments allowed us to reject the hypothesis that IFN-I hyperactivity caused the *sst1*-dependent AOD dysregulation. In contrast, they established that the hyperactivity of the IFN-I pathway in TNF-stimulated B6.Sst1S macrophages was itself driven by the *initial* dysregulation of iron storage and AOD, possibly via lipid peroxidation-dependent JNK activation. During prolonged TNF stimulation, however, the IFN-I pathway acted as a potent amplifier of lipid peroxidation.

4. Hyperactivity of Myc in susceptible macrophages after TNF stimulation fuels lipid peroxidation

We wanted to determine whether the AOD genes were regulated by the *sst1*-encoded genes directly or indirectly via an intermediary regulator. Previously, we identified two transcription factors whose activity was upregulated after 12h of TNF stimulation exclusively in the susceptible macrophages: Myc and HSF1 (*30*). The bulk RNA-seq analysis at this timepoint data also demonstrated the upregulation of Myc pathway along with E2F target genes, IFN-I and stress responses specifically in B6.Sst1 macrophages, as compared to B6 (**Fig.2**). The scRNA-seq analysis also demonstrated the association of Myc and stress response pathways in the mutant cells (**Fig.1**). Therefore, we hypothesized that in susceptible macrophages Myc might be involved in the dysregulation of AOD and iron storage.

First, we observed that Myc mRNA and protein were regulated in an *sst1*-dependent manner: in TNF-stimulated B6 BMDMs, Myc mRNA and protein levels were

initially increased and subsequently downregulated, while no downregulation was observed in the susceptible macrophages (**Fig.5A and B**). Next, we tested whether suppression of Myc activity could “normalize” the susceptible phenotype using Myc-Max dimerization inhibitor 10058-F4 (F4). Indeed, this treatment increased the levels of FTH and FTL proteins in TNF-stimulated susceptible macrophages (**Fig.5C**) and decreased the labile iron pool (**Fig.5D**). Accordingly, the levels of MDA, oxidized lipids and 4-HNE also significantly decreased (**Fig.5E – H, Suppl.Fig.5A**), as well as the levels of IFNβ, Rsad2 and the stress markers Trib3 and Chac1 (**Fig.5I**).

Next, we wanted to determine whether the upregulation of Myc is driven by TNF alone or in synergy with CSF1, a growth factor that also stimulates Myc. In vitro, we observed the upregulation of Myc shortly after the addition of fresh CSF1-containing media, but no difference in the Myc protein dynamics between B6 and B6.Sst1S BMDMs in the absence of TNF (**Suppl.Fig.5B**). Also, neither of three CSF1R inhibitors prevented the superinduction of IFNβ and Rsad2 mRNAs in B6.Sst1S macrophages induced by TNF (**Suppl.Fig.5C** and **D**). Because Myc induction by CSF1 and TNF is conducted via distinct relays of receptor signaling and transcription factors, we concluded that the *sst1* locus specifically controls Myc expression induced by inflammatory signaling. Indeed, Myc promoter has multiple predicted NF-κB and/or AP-1 transcription factors binding sites. To test this hypothesis, we used specific JNK inhibitor D-JNK1, but it had no effect on Myc upregulation in TNF-stimulated B6.Sst1S macrophages (**Fig.5J**). Thus, JNK activation in B6.Sst1S macrophages drives pathways downstream of Myc. The upstream Myc regulators remain to be found. Because both Sp110 and Sp140 mRNAs and proteins are highly upregulated during extended TNF

stimulation, one of them may participate in feedback regulation of TNF-induced Myc, either directly or via intermediates.

5. Myc hyperactivity and lipid peroxidation compromise the cell autonomous and T cell-mediated control of Mtb infection by B6.Sst1S macrophages.

Next, we wanted to text whether the described facets of the aberrant macrophage activation conferred by the *sst1S* allele were relevant to Mtb susceptibility. After macrophage infection with virulent Mtb in vitro, gradual accumulation of LPO product 4-HNE was observed in BMDMs of both B6 and B6Sst1S genetic backgrounds at 3 – 5 days post infection (dpi). It occurred either in the presence or absence of exogenous TNF (**Fig.6A - B,** and **Suppl.Fig.6A**). TNF stimulation tended to reduce the LPO accumulation in the B6 macrophages and to increase it in the B6.Sst1S ones (**Fig.6C**). Both Mtb-infected and non-infected B6.Sst1S macrophages accumulated 4-HNE suggesting that either TNF signaling or the diffusion of the low molecular weight 4-HNE may be responsible for the spread of LPO within the susceptible macrophage population (**Fig.6D**).

The inhibition of LPO production using Fer1 improved the survival of the Mtb-infected BMDMs (**Fig.6E**) and prevented the intracellular Mtb growth (**Fig.6F**) during the five-day in vitro infection. The iron chelator DFO also significantly reduced the Mtb growth, although restricting iron availability may directly affect the bacterial replication. Similarly, the survival of Mtb-infected BMDMs was improved, and the bacterial loads were significantly reduced by the Myc inhibitor, F4 (**Fig.6G and H**). Of note, the effects of the lipid peroxidation inhibitors became prominent between days 3 and 5 post

infection (**Suppl.Fig.6B**) suggesting that these inhibitors do not boost the bacterial killing by activated macrophages, but rather prevent macrophage damage caused by labile iron and lipid peroxidation.

Next, we tested whether the *sst1* susceptible allele compromised responsiveness of Mtb-infected macrophages to mycobacteria-specific T cells. The immune T cells were isolated from the regional lymph nodes of the resistant B6 mice vaccinated with live attenuated BCG vaccine, and added either to the B6 or B.Sst1S BMDM monolayers infected with Mtb the day before. The BMDMs were either treated with TNF prior to infection or not. After co-culture with the immune T cells for one or two days (**Suppl.Fig.6C** and **Fig.6I**, respectively), Mtb loads were significantly reduced in T cell co-cultures with the resistant B6 macrophages. The susceptible B6.Sst1S BMDMs did not respond to the same T cells either in the presence or absence of exogenous TNF (**Fig.6I** and **Suppl.Fig.6C**). Their responsiveness to T cells, however, was significantly improved by inhibitors of lipid peroxidation (Fer1) and Myc (F4): the bacterial loads were significantly reduced 24 and 48 h after co-culture with the immune T cells (**Fig.6J**). These data demonstrate that Myc hyperactivity and lipid peroxidation in B6.Sst1S macrophages compromise both the cell autonomous Mtb control after TNF stimulation, and also Mtb control in response to protective T cells induced by BCG vaccine.

Taken together, our in vitro studies demonstrate that Myc hyperactivity in activated macrophages results in the labile iron-mediated accumulation of toxic lipid peroxidation products leading to the aberrant macrophage activation, hyperactivity of IFN-I pathway and a loss of Mtb control. To evaluate their in vivo relevance, we compared TB progression in B6.Sst1S mice that were administered BCG vaccine 2

months after hock infection with Mtb. As shown in **Fig.6K**, BCG vaccine did not offer any protection to the B6.Sst1S mice. Of note, their resistant counterparts B6, did not develop progressive TB in this model, as reported elsewhere(*26*).

6. Loss of Mtb control in pulmonary TB lesions is associated with the accumulation of lipid peroxidation products and stress escalation in intralesional macrophages

We wanted to determine whether the aberrantly activated macrophages accumulate within TB lesions during progression of pulmonary TB in vivo. We used a mouse model of pulmonary TB where the lung lesions develop after hematogenous spread from the primary site of infection and progress exclusively in the lungs, despite systemic immunity and control of infection in other organs. Microscopic pulmonary lesions develop in the lungs of both B6 and B6.Sst1S mice, but subsequent progression occurs exclusively in the B6.Sst1S (*26*).

To detect the IFNβ-expressing cells within TB lesions, we introduced the Ifnβ-YFP reporter described previously (*60*) in the B6.Sst1S background. The B6.Sst1S,ifnb-YFP reporter mice were infected with virulent Mtb (*smyc'* :: mCherry) constitutively expressing the red fluorescent protein reporter (*61*). Lungs were collected 12 – 20 weeks post infection (wpi). After perfusion and fixation, 50 μm thick lung slices were prepared and stained using 4-HNE-specific antibodies. Following tissue clearing, 3D images were acquired using confocal microscopy.

Based on Mtb loads, TB lesions were classified in two categories: Mtb controlling paucibacillary lesions, and multibacillary lesions in which the control of Mtb growth was compromised (**Suppl.Fig.7**). Both types of lesions contained numerous YFP-expressing

cells **(Fig.7A)**. In paucibacillary lesions the 4-HNE accumulation was primarily associated with YFP-positive cells. The multibacillary lesions contained clusters of replicating Mtb and large swaths of 4-HNE-positive tissue, possibly due to diffusion of low molecular weight 4-HNE (**Fig.7A** and **Suppl.Fig.8A**). The 3D imaging demonstrated that YFP-positive cells were restricted to the lesions, but did not strictly co-localize with intracellular Mtb, i.e. the *Ifnb* promoter activity was triggered by inflammatory stimuli, but not by the direct recognition of intracellular bacteria. We validated the IFNβ reporter findings using in situ hybridization with the *Ifnb* probe, as well as anti-GFP antibody staining (**Suppl.Fig.8B-D**). These findings clearly demonstrate that local degradation of host defenses is associated with the accumulation of lipid peroxidation products and IFNβ expressing cells within advanced TB lesions.

Using co-staining with a macrophage-specific marker Iba1, we confirmed that the *Ifnb* reporter was primarily expressed by Iba1-positive myeloid cells (**Fig.7B**). To further characterize Iba1+ macrophages in TB lesions and identify pathways associated with advanced TB, we performed spatial transcriptomics analysis using the Nanostring GeoMX Digital Spatial Profiler (DSP) system(*62*)(**Suppl.Fig.9**). Comparing Iba1+ gene expression profiles in the mutibacillary vs paucibacillary lesions, we identified 192 upregulated and 376 downregulated genes at a two and above fold change (**Suppl.Table 7**). Pathway analysis demonstrated a highly significant upregulation of Hypoxia, TNF and IL6/STAT3 Signaling, Glycolysis, Complement and Coagulation pathways in the multibacillary lesions consistent with the escalation of hypoxia, inflammation and macrophage activation in the advanced lesions. Mechanistically, top

transcription factors associated with genes upregulated in the multibacillary lesions were NFKB1, JUN, STAT1, STAT3 and SP1 (**Suppl.Fig.10A-C**).

To specifically interrogate the interferon pathways in paucibacillary vs multibacillary lesions, we compiled a list of 430 interferon type I and type II inducible genes from public databases that were also included in Nanostring Whole Transcriptome Analysis (WTA) probes. Among these, 70 genes were differentially regulated between the Iba1+ macrophages in multi- vs paucibacillary lesions (**Fig.7C**). Among the upregulated genes were metalloprotease Mmp12, IL6 and Socs3, chemokines Cxcl10, Ccl2, Ccl3, Ccl4, Ccl19, cell stress and senescence marker p21 (Cdkn1a), and many known IFN-I target genes. The most upregulated pathways in Iba1+ cells within multibacillary lesions were Interferon, TNF, and IL6/STAT3 Signaling, and top transcription factors associated with upregulation of these pathways were NFKB1, STAT3, STAT1 and IRF1. Among the IFN-inducible genes upregulated in paucibacillary lesions were Ifi44l, a recently described negative regulator of IFN-I that enhances control of Mtb in human macrophages(*63, 64*) and Ciita, a regulator of MHC class II inducible by IFNγ, but not IFN-I (**Suppl.Table 8** and **Suppl.Fig.10 D-E**). Thus, progression of pulmonary TB and loss of local Mtb control within the lung lesions was associated with the accumulation of aberrantly activated macrophages that contained lipid peroxidation products, with upregulation of the IFN-I pathway and downregulation of IFNγ-inducible genes.

Using fluorescent multiplexed immunohistochemistry (fmIHC), we compared the upregulation of stress markers phospho-cJun and Chac1 (**Fig.7D** and **Suppl.Fig.11** and **12**). In the advanced lesions these markers were primarily expressed by activated

macrophages (Iba1+) expressing iNOS and/or Ifnβ (YFP+)(**Fig.7E**). We also documented the upregulation of PKR in the multibacillary lesions, which is consistent with the upregulation of the upstream IFN-I and downstream Integrated Stress Response (ISR) pathways, as described in our previous studies (*30*) (**Suppl.Fig.11B**).

Thus, progression from the Mtb-controlling paucibacillary to non-controlling multibacillary TB lesions in the lungs of TB susceptible mice was mechanistically linked with a pathological state of macrophage activation characterized by escalating stress (as evidenced by the upregulation phosph-cJUN, PKR and Chac1), the upregulation of IFNβ and the IFN-I pathway hyperactivity, with a concurrent reduction of IFNγ responses.

Discussion.

This study reveals novel upstream mechanisms that trigger and maintain hyperactivity of the IFN-I pathway in activated macrophages and demonstrates their relevance to pulmonary TB. First, we found that the hyperactivity of the IFN-I pathway was a part of a broader dysfunctional macrophage activation leading to unresolving stress and loss of Mtb control. Second, we have shown that oxidative stress in TNF-activated macrophages was sufficient to boost IFNβ expression, and it did not require the recognition of either the endogenous or Mtb-derived nucleic acids. Third, we demonstrated that accumulation of aberrantly activated, stressed macrophages within TB lesions, but not their death, preceded tissue necrosis and exuberant Mtb growth. Thus, in the mouse model that recapitulate key pathomorphological features of pulmonary TB in human patients, the aberrant macrophage activation state was responsible for both the inflammatory tissue damage and the failure of local immunity.

Previous studies demonstrated that inactivating the IFN-I pathway by IFN receptor knockout in B6.Sst1S background increased resistance to Mtb infection in vivo but did not restore it to the wildtype B6 level (*31*). Thus, the superinduction of IFNβ alone was insufficient to completely account for the *sst1*-mediated cell autonomous macrophage phenotype. Comparing the pseudotime trajectories of the B6 and B6.Sst1S macrophages during prolonged TNF stimulation, we found upregulation of anti-oxidant defense genes in the wild type B6 macrophages, while, in contrast, B6.Sst1S BMDMs demonstrated superinduction of IFNβ and IFN-I pathway genes. Using real time-course experiments, we found that this divergence occurs 8 - 12h after TNF stimulation, i.e. the time interval during which the Sp110 and Sp140 genes and proteins are upregulated

exclusively in the wild type cells. By 12 h of TNF stimulation, the B6.Sst1S mutant macrophages displayed the dysregulated activation of AOD concomitantly with the upregulation of heat shock proteins and the increased activity of HSF1 described previously (*30*). Blockade of IFNAR1 did not prevent the initial AOD dysregulation during this period suggesting that the dysregulated oxidative stress response of B6.Sst1S macrophages was upstream of the IFN-I pathway hyperactivity. Indeed, blocking lipid peroxidation using Fer-1 or an iron chelator prevented the IFNβ superinduction. This conclusion was also supported by recent in vivo experiments in which antioxidant defense in B6.Sst1S mice was enhanced by knockout of the Bach1 gene – a negative regulator of NRF2 (*65*). After Mtb infection, the B6.Sst1S,Bach1-/- mice displayed reduced lung inflammatory damage and decreased expression of the IFN-I pathway genes, as compared to the B6.Sst1S mice(*65*). Previously, we reported that the IFNβ super-induction in the *sst1*-susceptible macrophages was driven by the synergy of TNF/NFκB and stress-activated kinase JNK pathways (*30*). In this study we demonstrated that JNK activation was sustained at higher levels in the B6.Sst1S macrophages after 12 h of TNF stimulation. We hypothesize that autocatalytic lipid peroxidation may be a major factor sustaining the unresolving stress and stress-kinase activation during prolonged stimulation of the B6.Sst1S macrophages with TNF.

This model is consistent with an unbiased computational approach that considered genes co-regulated with Sp110 and Sp140 in mouse macrophage datasets that independently suggested their primary association with anti-oxidant response pathways. Experimentally, we found that Sp110 and Sp140 deficiency in activated macrophages led to the partial AOD dysregulation: a coordinated downregulation of

ferritin light and heavy chains mRNAs, as well as the genes of the glutathione and thioredoxin antioxidant systems and NADPH regeneration that are involved in restoring redox balance and preventing lipid peroxidation. Free ferrous iron (Fe^{+2}) catalyzes the intracellular peroxidation of polyunsaturated fatty acids (PUFA) via the Fenton reaction that in the absence of terminators, can proceed in an autocatalytic manner in cell membranes containing tightly packed PUFA (*66*). Indeed, the prolonged TNF stimulation of the *sst1* mutant macrophages led to increased labile iron pool and the accumulation of toxic low molecular weight lipid peroxidation products MDA and 4-HNE. Unlike ferroptosis, however, this did not result in massive cell death, but led to persistent unresolving stress and an aberrant state of macrophage activation.

Exploring potential mechanisms of the AOD dysregulation in B6.Sst1S macrophages, we found that the upregulation of NRF2 protein after TNF stimulation was impaired, although the Nrf2 mRNA levels were induced to higher levels in comparison to the B6 macrophages. This effect could not be explained by differences in the kinetics of NRF2 protein degradation suggesting that the *sst1* locus may regulate the NRF2 protein levels post-transcriptionally, either at the levels of Nrf2 mRNA splicing or translation, as suggested by(*67-70*). The growing body of experimental evidence suggest that a specialized translation machinery is involved in context-dependent regulation of protein biosynthesis(*71*). Ribosome modifications, such as protein composition and rRNA methylation, were shown to be involved in control of selective IRES-dependent translation in myeloid cells(*72, 73*) and regulation of inflammation(*74-76*). Recently, enrichment of SP100 and SP110 proteins in ribosomes was observed during B6 macrophage activation with LPS(*77*). These findings suggest that the SP110

protein may be involved in fine tuning of protein biosynthesis in activated macrophages favoring the IRES-dependent NRF2 translation.

More broadly, we hypothesize that in activated macrophages the SP110 and SP140 proteins serve as context-dependent regulators of macrophage stress resilience. In addition to transcriptional regulation by interferons, their activities can by tuned by i) inflammatory stimuli via CARD domain(*78*), ii) metabolism, via the activated nuclear receptor interaction domain LXXLL, and potentially, iii) intracellular nucleic acids via the DNA interaction domain SAND. In addition, the SP140 protein contains C terminal chromatin binding PHD and BRD domains that are most likely explain its unique role in chromatin regulation and suppression of illegitimate transcription. The upregulation and stabilization of these proteins would promote terminal differentiation, stress adaptation and functional fitness of activated macrophages.

To explain how the SP110 and SP140 regulate macrophage activation, we propose the following model (**Fig.8**). In actively growing cells, Myc promotes ribosome biogenesis, cap-dependent protein translation and also suppresses expression of FTH, most likely to provide labile iron for anabolic metabolism(*51, 79*). By inhibiting Myc in activated macrophages, SP140 may facilitate the SP110-mediated NRF2 translation, and the upregulation of ferritin proteins to sequester free iron. Thus, their combined effects would lead to fine tuning of macrophage activation within inflammatory microenvironments and increased stress resilience. Recent in vivo studies demonstrated that, indeed, ferritins and antioxidant pathways were upregulated in inflammatory macrophages isolated from Mtb-infected wild type B6 mice (*80*). In contrast, during prolonged TNF stimulation of the B6.Sst1S macrophages, Myc

hyperactivity and the impairment of AOD lead a coordinated downregulation of the Ferritin heavy and light chains and lipid peroxidation inhibitor genes. This initiates an autocatalytic lipid peroxidation that fuels persistent oxidative stress and, likely, sustains the activity of JNK. Downstream, IFNβ superinduction in B6.Sst1S macrophages leads to the upregulation of interferon-inducible genes, including PKR. The subsequent PKR-dependent ISR activation leads to the upregulation of Chac1(*30*) - a glutathione degrading enzyme gamma-glutamylcyclotransferase 1(*81*) that further compromises the AOD. This stepwise escalation eventually locks the susceptible macrophages in a state of unresolving stress which is maintained by continuous stimulation with TNF and IFN-I.

Contrary to our findings, a recent in vivo study demonstrated that early Mtb growth after aerosol infection is reduced in NRF2 knockout mice (*82*) possibly due to decrease anti-oxidant defense and a concordant increase in intracellular free radicals. A similar effect was found due to inactivation of ALDH2, an enzyme that inactivates aldehydes - toxic low molecular weight end products of lipid peroxidation. The ALDH2 knockout in B6.Sst1S mice reduced the bacterial loads during an acute phase of TB(*83*). In contrast, studies by Amaral et al. demonstrated that after high dose Mtb infection massive accumulation of lipid peroxidation products leads to necrosis of pulmonary TB lesions and macrophage ferroptosis (*84*), while boosting antioxidant defense by Bach1 knockout improves the outcomes of TB infection in both B6 and B6.Sst1S mice (*65*).

Here, we also demonstrate that free radicals formed via iron-mediated lipid peroxidation damaged activated B6.Sst1S macrophages and, eventually reduced their ability to control Mtb both in a cell autonomous and a T cell-dependent manner. In the

mouse model of chronic TB infection, the accumulation of lipid peroxidation products within the lesion did not appear to significantly affect the long term Mtb survival. Mycobacterial cell wall and multiple mycobacterial antioxidant pathways exist to allow for the survival of, at least, a fraction of mycobacterial population in highly oxidative environments (*85, 86*). The self-inflicted oxidative damage, however, gradually degraded the macrophage population to a degree that allowed for Mtb replication, and eventually provided a fodder for growing mycobacteria(*87*).

In vivo, monocytes recruited to inflammatory lesions may be particularly vulnerable to the dysregulation of Myc. Prior to terminal differentiation within inflammatory milieu, these immature cells undergo several cycles of replication. Cell growth requires labile iron that is provided by Myc via downregulation of ferritins(*51, 57*). Recently we found that lung epithelial cells embedded within TB lesions express CSF1 – a macrophage growth factor known to stimulate Myc expression (*26*). Thus, the CSF1 – Myc axis may synergize with TNF to initiate and propagate the aberrant activation state in monocytes recruited to chronic pulmonary TB lesions. Similarly, growth factors produced locally within inflamed tissues may sustain Myc hyperactivity and the aberrant activation state of monocytes/macrophages in other chronic inflammatory pathologies.

In conclusion, the *sst1* mutant mice lacking the SP110 and SP140 proteins reveal a novel macrophage activation state shaped by the collision of anabolic (Myc), homeostatic (antioxidant defense and proteostasis), and immune pathways (TNF and type I IFN). Although this persistent activation state is damaging for macrophages and potentially suicidal, it may boost macrophage-mediated resistance to acute infections. By coordinately increasing free iron pool for non-enzymatic free radical generation, and

simultaneously decreasing the buffering capacity of intracellular antioxidants, this activation state promotes generation and unopposed spread of free radicals. More broadly, it may facilitate the interferon-mediated elimination of the aberrantly activated cells to prevent their oncogenic transformation (*88, 89*). Perhaps, in addition to SP110/140 proteins other intracellular sensors and tunable controllers mediate the initiation and maintenance of this cell state. However, the inappropriate activation of its build-in amplification mechanisms may drive immunopathologies in the face of chronic stimulation as occurs with Mtb infection. Further understanding the signals and checkpoints that regulate this cell state is necessary for its rational therapeutic modulation to boost host defenses and mitigate the collateral tissue damage.

Material and Methods:

Reagents

Recombinant mouse TNF (Cat# 315-01A) and IL-3 (Cat# 213-13) were procured from Peprotech. The mouse monoclonal antibody to mouse TNF (MAb; clone XT22), isotype control, and mouse monoclonal antibody to mouse IFNβ (Clone: MAR1-5A3) were obtained from Thermo Scientific. BHA (Cat# B1253) and Deferoxamine mesylate (Cat#D9533]) were sourced from Sigma Aldrich. PLX3397 (Cat# S7818), Myc inhibitor (10058-F4) (Cat# S7153), Z-VAD-FMK (Cat# S7023), Necrostatin-1 (Cat# S8037), and ferrostatin-1 (Cat# S7243) were purchased from Selleckchem. D-JNK1 (Cat# HY-P0069), GW2580 (Cat# HY-10917), and BLZ945 (Cat# HY-12768) were acquired from Med Chem Express. Fetal bovine serum (FBS) for cell culture medium was sourced from HyClone. Middlebrook 7H9 and 7H10 mycobacterial growth media were purchased from BD and prepared following the manufacturer's instructions. A 50 mg/mL hygromycin solution was utilized for reporter strains of Mtb Erdman (SSB-GFP, smyc′::mCherry).

Animals

C57BL/6J inbred mice were obtained from the Jackson Laboratory (Bar Harbor, Maine, USA). The B6J.C3-*Sst1*$^{C3HeB/Fej}$ Krmn congenic mice were created by transferring the *sst1* susceptible allele from C3HeB/FeJ mouse strain on the B6 (C57BL/6J) genetic background using twelve backcrosses (referred to as B6.Sst1S in the text). The B6.Sst1S,*ifnb*-YFP mice were produced by breeding B6.Sst1S mice with a reporter

mouse containing a Yellow Fluorescent Protein (YFP) reporter gene inserted after the *Ifnb1* gene promoter (*60*). The YFP serves as a substitute for Interferon beta (IFNβ) gene expression. All experiments were performed with the full knowledge and approval of the Standing Committee on Animals at Boston University in accordance with relevant guidelines and regulations.

BMDMs culture and Treatment

The isolation of mouse bone marrow and the cultivation of bone marrow-derived macrophages (BMDMs) were conducted following the procedures outlined in a prior study (*90*). BMDMs were plated in tissue culture plates, followed by treatment with TNF and incubation for 16 hours at 37°C with 5% CO2. Various inhibitors were applied to the cells until the point of harvest.

Infection of BMDM with *M. tuberculosis*

For infection experiments, M. tuberculosis H37Rv (Mtb) was cultured in 7H9 liquid media for three days and subsequently harvested. The bacteria were then diluted in media containing 10% L929 cell culture medium (LCCM) without antibiotics to achieve the desired Multiplicity of Infection (MOI). Following this, 100 µL of Mtb-containing media with the specified MOI was added to BMDMs cultivated in a 96-well plate format that had been pre-treated with TNF or inhibitors. The plates underwent centrifugation at 500xg for 5 minutes, followed by an incubation period of 1 hour at 37°C. To eliminate any extracellular bacteria, cells were treated with Amikacin at 200 µg/µL for 45 minutes. Subsequently, cells were washed and maintained with inhibitors, as applicable, in

DMEM/F12 containing 10% FBS medium without antibiotics at 37°C in 5% CO2 for the duration of each experiment. Media changes and inhibitor replacements were carried out every 48 hours. The confirmation of MOIs was achieved by counting colonies on 7H10 agar plates. All procedures involving live Mtb were conducted within Biosafety Level 3 containment, adhering to regulations from Environmental Health and Safety at the National Emerging Infectious Disease Laboratories, the Boston Public Health Commission, and the Center for Disease Control.

Cytotoxicity and Mycobacterial growth assays

The cytotoxicity, cell loss, and Mtb growth assays were conducted in accordance with the procedures outlined by (*90*). In brief, BMDMs were subjected to inhibitor treatment or Mtb infection as previously described for specified time points. Upon harvesting, samples were treated with Live-or-Dye™ Fixable Viability Stain (Biotium) at a 1:1000 dilution in 1X PBS/1% FBS for 30 minutes. Following staining, samples were carefully washed to prevent any loss of dead cells from the plate and subsequently treated with 4% paraformaldehyde (PFA) for 30 minutes. After rinsing off the fixative, samples were replaced with 1X PBS. Following decontamination, the sample plates were safely removed from containment. Utilizing the Operetta CLS HCA System (PerkinElmer), both infected and uninfected cells were quantified. The intracellular bacterial load was assessed through quantitative PCR (qPCR) employing a specific set of Mtb and *M. bovis*-BCG primer/probes, with BCG spikes included as an internal control, as previously described(*90*).

RNA Isolation and quantitative PCR

The extraction of total RNA was carried out utilizing the RNeasy Plus mini kit (Qiagen). Subsequently, cDNA synthesis was conducted using the Invitrogen™ SuperScript™ III First-Strand Synthesis SuperMix (Cat#18080400). Real-time PCR was executed with the GoTaq qPCR Mastermix (Promega) employing the CFX-96 real-time PCR System (Bio-Rad). Oligonucleotide primers were designed using Integrated DNA Technologies. Either 18S or β-actin expression served as an internal control, and the quantification of fold induction was computed using the ddCt method.

Analysis of RNA sequencing data

Raw sequence reads were mapped to the reference mouse genome build 38 (GRCm38) by STAR (*91*). The read count per gene for analysis was generated by featureCounts (*92*). Read counts were normalized to the number of fragments per kilobase of transcript per million mapped reads (FPKM) using the DESeq2 Bioconductor R package (*93*). Pathway analysis was performed using the GSEA method implemented in the camera function from the limma R package (*94*). Databases KEGG, MSigDB Hallmark, Reactome were used for the GSEA analysis . Transcripts expressed in either 3 conditions with FPKM > 1 were included in the pathway analyses. To infer mice macrophage gene regulatory network, we used ARCHS4 collected list of RNE-seq data for mice macrophages cells from Gene Expression Omnibus (GEO) (*95*). The total number of analyzed experimental datasets was 1960. This gene expression matrix was utilized as input for the GENIE3 algorithm, which calculated the most likely co-expression partners for transcription factors. The list of transcription factors was derived

from the Animal TFDB 3.0 database (*96*). The Virtual Inference of Protein Activity by Enriched Regulon Analysis (VIPER) algorithm was used to estimate the prioritized list of transcription factors (*97*). The software Cytoscape (version 3.4.0) was used for network visualization (*98*). The i-cisTarget web service was used to identify transcription factor binding motifs that were over-represented on a gene list (*99*). Statistical analysis and data processing were performed with R version 3.6.1 (https://www.r-project.org/) and RStudio version 1.1.383 (https://www.rstudio.com).

Generation and sequencing of single-cell RNA libraries

Single cell suspensions of mouse bone marrow derived macrophages were loaded on a 10X genomics chip G at concentrations varying between 1,240,000 – 1,575,000 cells/mL aiming for a targeted cell recovery of 5,000 cells per sample and processed using the 10X Genomics 3'v3.1 Dual index kit according to the manufacturer protocol (10x Genomics, CA, USA). Following the 10X Genomics Chromium controller run the Gel-beads in emulsion (GEMs) were transferred to strip tubes and subsequently put into a thermal cycler using the following parameters: 45 min at 53 °C, 5 min at 85 °C, hold at 4 °C. The samples were then stored in a -20˚C freezer overnight. The next day samples were thawed at room temperature before adding the recovery agent to break the GEMs. Subsequently the cDNA was purified and amplified, and the gene expression libraries were generated and purified. The size distribution and molarity of these libraries were assessed using the Bioanalyzer High Sensitivity DNA Assay (Agilent Technologies, Lexington, MA, USA). The libraries were then pooled at 5nM and sequenced on an

Illumina NextSeq 2000 instrument at a 600pM input and 2% PhiX spike in using a P3 100 cycle flow cell (Illumina, San Diego, CA, USA) resulting in 36000-58000 reads per cell.

Processing of scRNA-seq data

The 10x Genomics Cell Ranger pipeline v6.0.1 was used for demultiplexing, alignment, identification of cells, and counting of unique molecular indices (UMIs). The Cell Ranger mkfastq pipeline was used to demultiplex raw base call (BCL) files generated by Illumina sequencers into FASTQ files. The Cell Ranger count pipeline was used to perform alignment and create UMI count matrices using reference genome mm10 (Ensembl 84) and parameters –expect-cells = 5000. Droplets with at least 500 UMIs underwent further quality control with the SCTK-QC pipeline(*100*). The median number of UMIs was 9,927, the median number of genes detected was 2,637, the median percentage of mitochondrial reads was 5.43%, and the median contamination estimated by decontX was 0.17 across cells from all samples(*101*). Cells with less than 500 counts, less than 500 genes detected, or more than 25% mitochondrial counts were excluded leaving a total of 14,658 cells for the downstream analysis.

Clustering of single-cell data

The Seurat package was used to cluster the cells into subpopulations(*102*). The 2,000 most variable genes were selected using the FindVariableFeatures function, after removing features with fewer than 3 counts in 3 cells. Cells were embedded in two

dimensions with UMAP using the RunUMAP function. The clustering was performed at resolution 0.8 resulting in 15 clusters. Markers for each cluster were identified with the FindAllMarkers function using the Wilcoxon Rank Sum test and default parameters: log fold-change threshold = 0.25 and min.pct = 0.1. The trajectory analysis was performed using the slingshot package; the pseudotime trajectory was computed using the slingshot function and selecting the PCA and unweighted cluster labels as inputs(*103*). The pathway analysis was performed using the VAM package in combination with MSigDB's Hallmark geneset collection. The genesets were scored using the vamForSeurat function, and the top pathways were found by running the FindAllMarkers analysis on the CDF assay.

Western Blot Analysis

Equal amounts of protein extracts were separated by SDS-PAGE and transferred to a PVDF membrane (Millipore). Following a 2-hour blocking period in 5% skim milk in TBS-T buffer [20 mM Tris-HCl (pH 7.5), 150 mM NaCl, and 0.1% Tween20], the membranes were incubated overnight with the primary antibody at 4°C. Subsequently, bands were visualized using the chemiluminescence (ECL) kit (Thermo Scientific). A loading control, either β-actin or β-tubulin, was assessed on the same membrane. Secondary antibodies used included HRP-conjugated goat anti-mouse and anti-rabbit antibodies.

Half-life determination of NRF2 protein.

The B6 and B6.Sst1S BMDM were stimulated with TNF (10 ng/ml) for 6 h. Cycloheximide (2 uM) was added to the cultures and cells were harvested after 15, 30,

45, 60, 90, and 120 min. Western blotting was carried out for NRF2 and β-tubulin as described. The densitometry analysis was performed using ImageJ software (NIH, USA). The linear regression curve was plotted using GraphPad Prism software, and the half-life of NRF2 protein was derived."

Electrophoretic Mobility Shift Assay

The nuclear extracts were prepared using a nuclear extraction kit (Signosis Inc.) according to the instructions provided. The EMSA was carried out using the EMSA assay kit (Signosis Inc.) following the instructions provided. Briefly, 5 mg of nuclear extract was incubated with biotin-conjugated NRF2 (ARE) probe in 1X biding buffer for 30 min. The reaction mixture was electrophoresed in 6.5% non-denaturing polyacrylamide gel and then blotted onto a nylon membrane. The protein-bound probe and free probe were immobilized on the membrane by UV light mediated cross-linking. After blocking the membrane, the probes were detected using streptavidin-HRP mediated chemiluminescence method. The images were captured using ImageQuant LAS 4000.

Quantification of intracellular labile iron

The method used to measure Labile Intracellular Iron (LIP) involved the Calcein acetoxymethyl (AM) ester (Invitrogen) quenching technique with some modifications, as described in (*84, 104, 105*). BMDMs were plated in 96 well plates and washed with 1× DPBS before being lysed with 0.05% saponin for 10 minutes. Next, the cell lysates were incubated with 125 nM calcein AM at 37°C for 30 minutes. A negative control was

established by incubating the lysates with the iron chelator deferoxamine (Sigma-Aldrich) at room temperature for 30 minutes, while FeSO4-treated cells served as the positive control. The fluorescence of Calcein AM was measured using a fluorescence microplate reader, and the differential MFI of calcein AM between untreated and deferoxamine-treated samples was calculated to determine intracellular labile iron and represented as fold change.

MDA assay

The amount of MDA in the BMDMs were measured using a Lipid Peroxidation (MDA) Assay Kit (Abcam, ab118970) according to the manufacturer's protocols. Briefly, $2x10^6$ cells were lysed in Lysis Solution containing butylated hydroxytoluene (BHT). The insoluble fraction was removed by centrifugation, and the supernatant was collected, protein concentrations were estimated and used for analysis. The equal amount of supernatants (Based on protein concentration) were mixed with thiobarbituric acid (TBA) solution reconstituted in glacial acetic acid and then incubated at 95˚C for 60 min. The supernatants containing MDA-TBA adduct were added into a 96-well microplate for analysis. A microplate reader was used to measure the absorbance at OD 532 nm.

Lipid peroxidation by C11-Bodipy 581/591

Briefly, the cells were washed 3 times with 1X PBS and treated with 1 μM C11-Bodipy 581/591 dye (Invitrogen) suspended in 1X PBS for 30 min in the dark at 37oC. The LPOs were measured fluorometrically using Spectramax M5 microplate reader (Molecular Devices).

Measurement of total antioxidant capacity

The total antioxidant capacity was quantified using the Antioxidant assay kit (Cayman chemical) according to the instructions provided. A standard curve was generated by using various concentrations of Trolox (0.068-0.495 mM). 10 mg of the cell lysate was used to determine the Trolox equivalent antioxidant capacity. The percentage of induced antioxidant capacity was calculated using the formula, (Trolox equivalent$_{TNF\ stimulated}$-Trolox equivalent$_{unstimulated}$)/ Trolox equivalent $_{unstimulated}$ X 100.

Immunofluorescence imaging

BMDMs were cultured on coverslips and subjected to treatment with or without TNF, followed by processing for inhibitor treatment or Mtb infection. Subsequently, cells were fixed with 4% paraformaldehyde (PFA) for 10 minutes (non-infected) or 30 minutes (Mtb infected) at room temperature and then blocked for 60 minutes with 1% BSA containing 22.52 mg/mL glycine in PBST (PBS + 0.1% Tween 20). After the blocking step, cells were incubated overnight with primary antibodies (4HNE, NRF2, or NRF-1), washed, and then incubated with Alexa Fluor 594-conjugated Goat anti-Rabbit IgG (H+L) secondary Antibody (Invitrogen) in 1% BSA in the dark for 1 hour. The cells were mounted using ProlongTM Gold antifade reagent (Thermo Fisher Scientific), and images were captured using an SP5 confocal microscope. All images were processed using ImageJ software.

Analysis of Small RNAs in Macrophages

Small RNA libraries were prepared from size fractionation of 10ug of total macrophage RNA on a denaturing polyacrylamide gel to purify 18-35nt small RNAs, and converted into Illumina sequencing libraries with the NEBNext Small RNA Library kit (NEB). Libraries were sequenced on the Illumina NextSeq-550 in the Boston University Microarray and Sequencing Core. We applied long RNAs and small RNAs RNAseq fastq files to a transposon and small RNA genomics analysis pipeline previously developed for mosquitoes (*58, 106*) with the mouse transposon consensus sequences loaded instead. Mouse transposon consensus sequences were downloaded from RepBase (*107*), and RNA expression levels were normalized internally to each library's depth by the Reads Per Million counting method.

Infection of mice with Mycobacterium tuberculosis and collection of organs

The subcutaneous infection of mice was conducted following the procedure outlined in (*26*). In brief, mice were anesthetized using a ketamine-xylazine solution administered intraperitoneally. Each mouse was subcutaneously injected in the hock, specifically in the lateral tarsal region just above the ankle (by placing the animal in the restrainer), with 50 µl of 1X PBS containing 10^6 CFU of Mtb H37Rv or Mtb Erdman (SSB-GFP, smyc′::mCherry). At the designated time points, the mice were anesthetized, lung perfusion was performed using 1X PBS/heparin (10 U/ml), and organs were collected.

Confocal immunofluorescence microscopy of tissue sections

Immunofluorescence of thick lung sections (50-100 µm) was conducted following the detailed procedures outlined earlier (*26*). Briefly, lung slices were prepared by

embedding formalin fixed lung lobes in 4% agarose and cutting 50 µm sections using a Leica VT1200S vibratome. Sections were permeabilized in 2% Triton X-100 for 1 day at room temperature, followed by washing and blocking with 3% BSA in PBS and 0.1% Triton X-100 for 1 hour. Primary antibodies were applied overnight at room temperature, followed by washing and incubation with secondary antibodies for 2 hours. Samples were stained with Hoechst solution for nuclei detection, cleared using RapiClear® 1.47 solution for 2 days, and mounted with ProLong Gold Antifade Mountant. Imaging was performed using a Leica SP5 spectral confocal microscope. Primary rabbit anti-4-HNE, anti-Iba1, and anti-iNOS polyclonal antibodies were detected using goat anti-rabbit antibodies labelled with Alexa Fluor 647.

Mycobacterial staining of lung sections

Paraffin-embedded 5µm sections were stained using New Fuchsin method (Poly Scientific R and D Corp., cat no. K093) and counterstained with methylene blue following the manufacturer's instructions.

Tissue inactivation, processing, and histopathologic interpretation

Tissue samples were submersion fixed for 48 h in 10% neutral buffered formalin, processed in a Tissue-Tek VIP-5 automated vacuum infiltration processor (Sakura Finetek , Torrance, CA, USA), followed by paraffin embedding with a HistoCore Arcadia paraffin embedding machine (Leica, Wetzlar, Germany) to generate formalin-fixed, paraffin-embedded (FFPE) blocks, which were sectioned to 5 µm, transferred to positively charged slides, deparaffinized in xylene, and dehydrated in graded ethanol. A

subset of slides from each sample were stained with hematoxylin and eosin (H&E) and consensus qualitative histopathology analysis was conducted by a board-certified veterinary pathologist (N.A.C.) to characterize the overall heterogeneity and severity of lesions.

Chromogenic Monoplex Immunohistochemistry

A rabbit specific HRP/DAB detection kit was employed (Abcam catalog #ab64261, Cambridge, United Kingdom). In brief, slides were deparaffinized and rehydrated, endogenous peroxidases were blocked with hydrogen peroxidase, antigen retrieval was performed with a citrate buffer for 40 minutes at 90°C using a NxGen Decloaking chamber (Biocare Medical, Pacheco, California), non-specific binding was blocked using a kit protein block, the primary antibody was applied at a 1.200 dilution, which cross-reacts with mycobacterium species (Biocare Medical catalog#CP140A,C) and was incubated for 1 h at room temperature, followed by an anti-rabbit antibody, DAB chromogen, and hematoxylin counterstain. Uninfected mouse lung was examined in parallel under identical conditions with no immunolabeling observed serving as a negative control.

Multiplex fluorescent immunohistochemistry (mfIHC)

A Ventana Discovery Ultra (Roche, Basel, Switzerland) tissue autostainer was used for brightfield and multiplex fluorescent immunohistochemistry (fmIHC). In brief tyramide signaling amplification (TSA) was used in an iterative approach to covalently bind Opal fluorophores (Akoya Bioscience, Marlborough, MA) to tyrosine residues in tissue

sections, with subsequent heat stripping of primary-secondary antibody complexes until all antibodies were developed. Before multiplex-IHC was performed, each antibody was individually optimized using a single-plex-IHC assay using an appropriate positive control tissue. Optimizations were performed to determine ideal primary antibody dilution, sequential order of antibody development, assignment of each primary antibody to an Opal fluorophore, and fluorophore dilution. Once an optimal protocol was established, 5µm tissue sections were cut from FFPE lung arrays. All Opal TSA-conjugated fluorophore reactions took place for 20 minutes. Fluorescent slides were counterstained with spectral DAPI (Akoya Biosciences) for 16 minutes before being mounted with ProLong gold antifade (ThermoFischer, Waltham, MA). Antibodies utilized in 4-plex 5 color (DAPI counterstained) analysis included: Iba1, iNOS, YFP, Chac1, and P-c-JUN. All rabbit antibodies were developed with a secondary goat anti-rabbit HRP-polymer antibody (Vector Laboratories, Burlingame, CA) for 20min at 37C and all mouse derived antibodies were developed with a secondary goat anti-mouse HRP-polymer antibody (Vector Laboratories).

Brightfield Immunohistochemistry

Antigen retrieval was conducted using a Tris based buffer-Cell Conditioning 1 (CC1)-Catalog # 950-124 (Roche). The MHCII primary was of mouse origin, so a goat anti-mouse HRP-polymer antibody (Vector Laboratories) was utilized. Brightfield slides utilized A ChromoMap DAB (3,3′-Diaminobenzidine) Kit-Catalog #760-159 (Roche) to form a brown precipitate at the site of primary-secondary antibody complexes containing HRP. Slides were counterstained with hematoxylin and mounted.

Multispectral whole slide microscopy

Fluorescent and chromogen labeled slides were imaged at 40X using a Vectra Polaris™ Quantitative Pathology Imaging System (Akoya Biosciences). For fluorescently labeled slides, exposures for all Opal dyes were set based upon regions of interest with strong signal intensities to minimize exposure times and maximize the specificity of signal detected. A brightfield acquisition protocol at 40X was used for chromogenically labeled slides.

Digitalization and linear unmixing of multiplex fluorescent immunohistochemistry

Whole slide fluorescent images were segmented into QPTIFFs, uploaded into Inform software version 2.4.9 (Akoya Biosciences), unmixed using spectral libraries affiliated with each respective opal fluorophore including removal of autofluorescence, then fused together as a single whole slide image in HALO (Indica Labs, Inc., Corrales, NM).

Quantitative analysis of immunohistochemistry

View settings were adjusted to allow for optimal visibility of immunomarkers and to reduce background signal by setting threshold gates to minimum signal intensities. After optimizing view settings, annotations around the entire tissue were created to define analysis area using the flood tool and artifacts were excluded using the exclusion pen tool. To analyze lesions independently, a tissue classifier that uses a machine-learning approach was utilized to identify lesions. The outputs from this classifier were annotations for each lesion, which were then isolated into independent layers, which

were analyzed separately from other layers. For quantifying myeloid markers in multiplexes, an algorithm called the HALO (v3.4.2986.151, Indica Labs, Albuquerque, NM, USA) Area Quantification (AQ) module was created and finetuned to quantify the immunoreactivity for all targets. Thresholds were set to define positive staining based on a real-time tuning feature. AQ outputted the percentage of total area displaying immunoreactivity across the annotated whole slide scan in micrometers squared (μm^2). AQ output the total percentage positive for each phenotype. AQ and HP algorithms were run across all layers for each individual lesion and exported as a .csv file.

Spatial transcriptomics

To perform spatial transcriptomics analysis we used the Nanostring GeoMX Digital Spatial Profiler (DSP) system (Nanostring, Seattle, WA) (*62, 108*). To identify pathways dominating early vs. late (advanced) lesions, we selected lungs from 2 mice with paucibacilarly early lesions and 2 mice with advanced multibacilarly lesions with necrotic areas. Slides were stained with fluorescent CD45-, pan-keratin-specific antibodies, and Iba1-specific antibodies (sc-32725, Santa Cruz Biotechnology, CA, USA) and DAPI. Diseased regions of interest (ROI) for expression profiling of Iba1+ cells were selected to focus on myeloid-rich areas avoiding areas of micronecrosis and tertiary lymphoid tissue (**Suppl.Fig.9**). Eight ROI each of normal lung, early and late lesions (respectively) were studied. The profiling used the Mouse Whole Transcriptome Atlas (WTA) panel which targets ~21,000+ transcripts for mouse protein coding genes plus ERCC negative controls to profile the whole transcriptome, excluding uninformative high expressing targets such as ribosomal subunits. A subsequent study focused on

gene expression within macrophages identified by Iba1 labeling in lung sections showing uncontrolled (advanced multibacillary) lesions in comparison to controlled (paucibacillary stage). Samples from each ROI were packaged into library for sequencing (NextSeq550, Illumina) following the procedure recommended by Nanostring. After sequencing, the data analysis workflow began with QC evaluation of each ROI based on thresholds for number of raw and aligned reads, sequencing saturation, negative control probe means, and number of nuclei and surface area. Background correction is performed using subtraction of the mean of negative probe counts. Q3 normalization (recommended by Nanostring) results in scaling of all ROIs to the same value for their 3rd quartile value. The count matrix was imported into the Qlucore Genomics Explorer software package (Qlucore, Stockholm, Sweden) and log2 transformed for further analysis. Statistical analysis was then performed to identify differentially expressed genes (typically unpaired t-test with Benjamini-Hochberg control for FDR rate at $q < .05$). Lists of differentially expressed genes (DEGs) from comparisons of distinct stages were further analyzed for enrichment of pathways or predicted transcription factors using the Enrichr online tool (*109-111*). To specifically explore interferon-related gene expression in Iba1+ macrophages, we used: 1) a list of genes unique to type I genes derived by pooling four common type I and type II interferon gene list respectively and identifying the non-overlapping (unique) genes for each type (see **Suppl.Table 8, Suppl. Fig. 10**); 2) using the GSEA analysis tool of the Qlucore software to evaluate enrichment of the MSigDB Hallmark collection of pathways (which include IFN-alpha and IFN-gamma, and other pathways of interest(*111*).

Statistical Analysis

To assess differences among multiple groups with two or more variables, we employed a two-way analysis of variance (ANOVA) with adjustments for multiple post hoc comparisons. Various comparisons were conducted in our study, encompassing comparisons among all groups, between the control group and all other groups, as well as between selected groups. In instances where multiple groups were compared with only one variable, a one-way ANOVA was utilized, and adjustments were made for multiple post hoc comparisons. When comparing only two groups, two-tailed paired or unpaired t-tests were employed, depending on the context. All statistical analyses were carried out using GraphPad Prism 9 software. Statistical significance was defined as a p-value < 0.05. Significance levels are indicated using asterisks (*, $P < 0.05$; **, $P < 0.01$; ***, $P < 0.001$; ****, $P < 0.0001$).

Resource availability

Lead contact

Further information and requests for resources and reagents should be directed to and will be fulfilled by the lead contact, Igor Kramnik (ikramnik@bu.edu).

Materials availability

All unique/stable reagents generated in this study are available from the Lead Contact with a completed Materials Transfer Agreement.

Data and code availability

This study did not generate datasets/code and any additional information will be available from the lead contact upon request.

Acknowledgement:

The authors would like to acknowledge expert support of Boston University Avedisian and Chobanian School of Medicine Sequencing and Single Cell Sequencing Cores. This work was supported by the National Institutes of Health grant R01HL126066 (to IK), R01HL133190 (to IK and WRB), National Institutes of Health grant R01CA244660 and EU grant no. 101136926 MULTIR" (to BK), and National Institutes of Health grant R01GM114864 (to AAG.). NIH grants R01-AG052465 and R01-GM135215 to NCL. National Library of Medicine grant R01LM013154 to JDC.

Author contributions

Conceptualization: IK, LK, SMY, WRB; Methodology : SMY, VZ, LK, OSR, AAG, YA, JDC, NAC, NCL, SL; Validation and formal analysis: SMY, SAA, VZ, OSR, AAG, BNK, LK, NCL, QM, GD; Investigation: SMY, PBA, SL, GD; Resources: IK, LK, AAG, BK, NCL, JDC, NAC; Writing – original draft: SMY, PBA, IK, LK; Writing – review & editing: IK, LK, WRB; Supervision: IK; Funding acquisition: IK, LK, AAG, BNK, NCL, WRB.

Declaration of interests

The authors have declared that no conflict of interest exists.

Inclusion and Diversity

We support inclusive, diverse, and equitable conduct of research.

Figure legends.

Figure 1. Single cell RNAseq analysis of the population dynamics of B6 and B6.Sst1S macrophages after TNF stimulation

A. Connectivity of AOD with the Myc-, NRF2-, JNK-, IFN-I-regulated pathways.

B. scRNA-seq analysis (UMAP) of B6 (R) and B6.Sst1S (S) BMDMs either naïve (R and S) or after 24 h of stimulation with TNF (RT and ST, respectively).

C. Expression of the sst1-encoded Sp110 and Sp140 genes in the population of either naïve (R) or TNF-stimulated (RT) B6 BMDMs.

D. Heatmap showing differentially expressed pathways in all cell clusters identified using scRNA-seq. Rows represent pathways and columns represent individual clusters with color intensity indicating the relative expression.

E. Reconstruction of the activation trajectories of TNF-stimulated resistant (RT) and susceptible (ST) macrophage populations using pseudotime analysis.

F. Heatmap showing differentially expressed pathways in subpopulations 1 to 5 identified using pseudotime analysis. Rows represents pathways and columns

represent individual subpopulations with color intensity indicating the relative expression.

G. Pathway heatmap representing transition from subpopulation 2 to unique subpopulation 3 in TNF-stimulated B6 macrophages.

H. The Sp110 and Sp140 gene regulatory network analysis. The mouse macrophage gene regulatory network was inferred using GENIE3 algorithm from mouse macrophages gene expression data sets obtained from Gene Expression Omnibus (GEO). First neighbors of Sp110/Sp140 genes were selected to infer a subnetwork of Sp110/Sp140 co-regulated genes. Green nodes represent transcription factors, blue nodes denote their potential targets.

Figure 2: Gene expression profiling comparing B6 and B6.Sst1.S BMDMs stimulated with TNF and regulation of NRF2.

A. Total levels of NRF2, NRF1, b-TrCP and Keap1 proteins in B6 and B6.Sst1S BMDMs stimulated with TNF (10 ng/ml) for 8, 12 and 24 h (Western blotting)

B. Cytoplasmic NRF2 and Bach1 proteins in B6 and B6.Sst1S BMDMs stimulated with TNF (10 ng/ml) for 8 and 12 h (Western blotting).

C. Nuclear NRF2 and Bach1 protein levels in B6 and B6.Sst1S BMDMs treated with TNF (10 ng/ml) for 8 and 12 h (Western blotting).

D and E. Confocal microscopy of NRF2 protein in B6 and B6.Sst1S BMDMs stimulated with TNF (10 ng/ml) for 12 h (scale bar 20 μm). Total NRF2 levels were quantified using ImageJ (E).

F. B6 and B6.Sst1S BMDMs were stimulated with TNF (10 ng/ml) for 8 h. The Nrf2 mRNA levels were quantified using quantitative RT-PCR.

G. Nuclear NRF2 binding to target sequence. Nuclear extracts were prepared from BMDMs treated with TNF (10 ng/ml) for 8 and 12 h. The binding activity of NRF2 was monitored by EMSA using biotin conjugated NRF2 specific probe (hot probe, red frames). Competition with the unconjugated NRF2 probe (cold probe) was used as specificity control.

H-I. The NRF2 protein stability in TNF-stimulated (10 ng/ml) B6 and B6.Sst1S BMDMs. BMDMs were stimulated with TNF. After 6 h, 25 μg/ml of cycloheximide (CHX) was added and cells were harvested after 15, 30, 45, 60, 90, ad 120 min. The NRF2 protein levels after TNF stimulation and degradation after cycloheximide addition were determined by Western blotting. I - Linear regression curves of NRF2 degradation after addition of CHX. Band intensities were measured by densitometry using ImageJ. No

significant difference in the NRF2 half-life was found: B6: 15.14 ± 2.5 min and B6.Sst1S: 13.35 ± 0.6 min.

J. Anti-oxidant genes co-regulated with Sp110 and Sp140 after stimulation with TNF (10 ng/ml) for 12 h. The heatmap was generated using FPKM values obtained from RNA-seq expression profiles of B6.Sst1S and B6 BMDMs after 12 h of TNF stimulation.

K. The heatmap of all genes related to response to oxidative stress (gene ontology category GO: 0006979). The heatmap was generated using FPKM values obtained using bulk RNAseq of B6.Sst1S and B6 BMDMs after 12 h of TNF stimulation. For heatmap generation, FPKM values were scaled using Z-scores for each tested gene.

The data represent the means ± SD of three samples per experiment, representative of three independent experiments.

The statistical significance was performed by two-way ANOVA using Tukey's multiple comparison test (Panels E-F). Significant differences are indicated with asterisks (*, $P < 0.05$; **, $P < 0.01$; ***, $P < 0.001$; ****, $P < 0.0001$).

Figure 3. Regulation of iron and lipid peroxidation in B6 and B6.Sst1.S BMDMs.

A and B. The expression of Fth and Ftl genes in B6 and B6.Sst1.S BMDMs treated with 10 ng/mL TNF for 12 and 24 h was determined using qRT-PCR.

C. The FTH and FTL protein levels in B6 and B6.Sst1.S BMDMs treated with 10 ng/mL TNF for 0, 12 and 24 h (FTH) and 0, 8, 12 and 24 h (for FTL) (Western blot).

D. The GPX1 and GPX4 protein levels in B6 and B6.Sst1.S BMDMs stimulated with TNF (10 ng/mL) for 0, 6, 12, and 24 h (Western blot).

E. The labile iron pool (LIP) in TNF-stimulated B6 and B6.Sst1.S BMDMs from were treated with 10 ng/mL TNF for 24 h. UT - untreated control. The LIP was determined using Calcein AM method and represented as fold change. DFO was used as negative control and FeSo4 was used as positive control.

F. The lipid peroxidation levels were determined by fluorometric method using C11-Bodipy 581/591. BMDMs from B6 and B6.Sst1.S were treated with 10 ng/mL TNF for 30 h. UT - untreated control.

G. Production of lipid peroxidation metabolite malondialdehyde (MDA) by B6 and B6.Sst1S BMDMs treated with 10 ng/mL TNF for 30 h. UT - untreated control.

H. The accumulation of the intracellular lipid peroxidation product 4-HNE in B6 and B6.Sst1.S BMDMs treated with 10 ng/mL TNF for 48 h was detected using 4-HNE specific antibody and confocal microscopy.

I. Inhibition of the 4-HNE accumulation in B6.Sst1.S BMDMs treated with TNF (10 ng/mL) for 48 h using IFNAR1 blocking antibodies. Isotype C Ab - isotype-matched negative control antibodies.

J. Inhibition of the 4-HNE accumulation in B6.Sst1.S BMDMs treated with 10 ng/mL TNF for 48 h using specific lipid peroxidation (ferroptosis) inhibitor, Fer-1 (10 μM). 4-HNE was detected using 4-HNE specific antibodies and confocal microscopy.

K. Cell death in B6 and B6.Sst1S BMDMs stimulated with 50 ng/mL TNF for 48 h. Percent of dead cells was determined by automated microscopy using Live-or-DyeTM 594/614 Fixable Viability stain (Biotium) and Hoechst staining.

L. Inhibition of cell death inhibition in B6.Sst1S BMDMs stimulated with 50 ng/mL TNF for 48 h using IFNAR1 blocking antibodies, Butylated hydroxyanisole (BHA) or Ferrostatin-1. Percent cell death was measured as in K.

The data represent the means ± SD of three samples per experiment, representative of three independent experiments.

The statistical significance was performed by two-way ANOVA using Bonferroni's multiple comparison test (Panel A, B, D, F, H and L) and Tukey's multiple comparison test (Panel E and I). Significant differences are indicated with asterisks (*, $P < 0.05$; **, $P < 0.01$; ***, $P < 0.001$; ****, $P < 0.0001$).

Figure 4. Crosstalk of the IFN-I and AOD pathways.

A. Blockade of IFNAR1 did not improve the upregulation of NRF2 in TNF-stimulated B6.Sst1.S macrophages during the initial 12 h of treatment. B6 and B6.Sst1S BMDMs were stimulated with 10 ng/mL TNF alone or in combination with IFNAR1 blocking antibodies or isotype control antibodies (Isotype C Ab) for 4, 8 and 12 h. The NRF2 protein levels were quantified using Western blot.

B. Blockade of IFNAR1 did not increase the FTL expression in TNF-stimulated B6.Sst1S BMDMs during the initial 12 h of TNF treatment. B6.Sst1S BMDMs were stimulated with 10 ng/mL TNF alone or in combination with IFNAR1 blocking antibodies or isotype control antibodies (Isotype C Ab) for 8 and 12 h. The FTL protein levels were quantified using Western blot.

C. Blockade of IFNAR1 did not increase the expression of Fth, Ftl and Gpx1 mRNAs. B6.Sst1.S BMDMs were treated with 10 ng/mL TNF alone or in combination with the IFNAR1 blocking antibodies or isotype control (Isotype C Ab) for 12 h. The mRNA expression levels were quantified using qRT-PCR.

D and E. Blockade of IFNAR1 inhibited the expression of Rsad2 (D), but not the Ifnβ(E) mRNAs. Expression of Rsad2 and Ifnβ was quantified using qRT-PCR after 16 h of TNF treatment.

F. Inhibition of lipid peroxidation prevented the superinduction of Ifnβ mRNA. B6.Sst1S BMDMs were stimulated with 10 ng/mL TNF for 2h, then the LPO inhibitor (Fer1) or iron chelator DFO were added for the remaining 14 h. The Ifnβ mRNA levels were quantified using qRT-PCR after 16 h of TNF stimulation.

G. Inhibition of TNF and lipid peroxidation reversed the Ifnβ mRNA superinduction after prolonged TNF stimulation. B6.Sst1S BMDMs were stimulated with 10 ng/mL TNF for 18h, then the anti-TNF Ab or LPO inhibitor (Fer1) were added for the remaining 12 h. The Ifnβ mRNA level was quantified using qRT-PCR after 30 h of TNF stimulation.

H. The B6 and B6.Sst1S BMDMs were treated with TNF (10 ng/ml) for 12, 24, and 36 h. The protein levels of phospho-cJun and phospho-ASK1 were determined using Western blot.

I. The TNF-induced c-Jun phosphorylation induced by TNF in B6.Sst1S BMDMs was inhibited by a highly specific JNK inhibitor. The B6 and B6.Sst1S BMDMs were treated with TNF (10 ng/ml) for 6, 12, and 24 h, in the presence or absence of D-JNK-1 (2 μM). The c-Jun phosphorylation was determined by Western blot.

The data represent the means ± SD of three samples per experiment, representative of three independent experiments.

The statistical significance was performed by two-way ANOVA using Sidak's multiple comparison test (Panel C-E) and Ordinary one-way ANOVA using Dunnett's multiple

comparison test (Panel F and G). Significant differences are indicated with asterisks (*, $P < 0.05$; **, $P < 0.01$; ***, $P < 0.001$; ****, $P < 0.0001$).

Figure 5. Myc dysregulation drives the aberrant state of macrophage activation.

A. The lack of Myc mRNA downregulation after prolonged TNF stimulation in B6.Sst1S macrophages. BMDMs from B6 and B6.Sst1.S were treated with 10 ng/mL TNF for 6, 12 and 24 h. Expression of Myc was quantified using qRT-PCR and expressed as a fold change compared to the untreated B6 BMDMs.

B. Myc protein levels expressed by B6 and B6.Sst1.S BMDMs during the course of stimulation with TNF(10 ng/mL) for 6 and 12 h. (Western blot).

C. Myc inhibition restored the levels of FTH and FTL proteins in TNF-stimulated B6.Sst1.S macrophages to the B6 levels. B6 and B6.Sst1.S BMDMs from were treated with 10 ng/mL TNF alone or in combination with Myc inhibitor, 10058-F4 (10 μM) for 24 h. 10058-F4 was added 2 h post TNF stimulation. Protein levels of FTH and FTL were quantified using Western blot.

D. Myc inhibition decreased the labile iron pool in TNF-stimulated B6.Sst1.S macrophages. B6.Sst1.S BMDMs were treated with 10 ng/mL TNF or left untreated for 48 h. The 10058-F4 inhibitor was added 2 h post TNF stimulation. The labile iron pool

(LIP) was measured using Calcein AM method and represented as fold change. DFO was used as negative control and FeSo4 was used as positive control.

E and F. Myc inhibition reduced lipid peroxidation in TNF-stimulated B6.Sst1S BMDMs. Cells were treated with 10 ng/mL TNF in presence or absence of 10058-F4 for 48 h. The inhibitor was added 2 h post TNF stimulation. The MDA production was measured using commercial MDA assay (E). The lipid peroxidation was measured by fluorometric method using C11-Bodipy 581/591 (F).

G and H. B6.Sst1.S BMDMs were treated as above The accumulation of lipid peroxidation product, 4HNE after 48h was detected by confocal microscopy using 4-HNE specific antibody. The 4HNE accumulation was quantified using ImageJ and plotted as fold accumulation compared to untreated group (G).

I. BMDMs from B6.Sst1.S were treated with 10 ng/mL TNF alone or in combination with Myc inhibitor, 10058-F4 (10 μM) for 24 h. 10058-F4 was added 2 h post TNF stimulation. Expression of Ifnβ, Rsad2, Trib3 and Chac1 were quantified using qRT-PCR.

J. B6.Sst1S BMDMs were treated with TNF (10 ng/ml) for 6, 12, and 24 h in the presence or absence of JNK inhibitor D-JNK1 (2 μM). The cells were harvested and the protein levels of c-Myc and p-cJun were determined by western blotting.

The data represent the means ± SD of three samples per experiment, representative of three independent experiments.

The statistical significance was performed by two-way ANOVA using Bonferroni's multiple comparison test (Panel A) and ordinary one-way ANOVA using Dunnett's multiple comparison test (Panel D-G and I). Significant differences are indicated with asterisks (*, $P < 0.05$; **, $P < 0.01$; ***, $P < 0.001$; ****, $P < 0.0001$).

Figure 6. Myc and lipid peroxidation compromise control of intracellular Mtb by the B6.Sst1 macrophages.

A-C. Accumulation of 4-HNE in Mtb-infected B6 and B6.Sst1.S macrophage monolayers infected with Mtb. BMDMs were either treated with 10 ng/mL TNF or left untreated (UT), and subsequently infected with Mtb at MOI=1. 4-HNE was detected by confocal microscopy using 4-HNE specific antibody 3 and 5 dpi. The 4HNE accumulation was quantified at 5 dpi using ImageJ and plotted as fold accumulation compared to untreated B6 (UT).

D. Naïve and TNF-stimulated B6.Sst1.S BMDMs were infected with Mtb Erdman reporter strain (SSB-GFP, smyc'::mCherry) . The accumulation of 4HNE was detected in both Mtb-infected and non-infected cells.

E and F. LPO inhibition improves the survival and Mtb control by B6.Sst1.S macrophages. BMDMs were treated with 10 ng/mL TNF alone in combination with Fer-1

(3 μM) or DFO (50 μM) for 16 h and subsequently infected with Mtb at MOI=1. At days 1 and 5 post infection, total cell numbers were quantified using automated microscopy (E) and M.tb loads was determined using a qPCR-based method (F).

G and H. Myc inhibition improves the survival and Mtb control by B6.Sst1.S macrophages. BMDMs were treated with 10 ng/mL TNF alone or in combination with 3 μM or 10 μM 10058-F4 for 16 h and subsequently infected with Mtb at MOI=1. At days 1 and 5 post infection, total cell numbers were quantified using automated microscopy (G) and M.tb loads was determined using a qPCR-based method (H).

I. Differential effect of BCG-induced T cells on Mtb control by B6 and B6.Sst1.S macrophages. BMDMs of both backgrounds were treated with 10 ng/mL TNF or left untreated and subsequently infected with Mtb at MOI=1. T lymphocytes purified from lymph nodes of BCG vaccinated B6 mice were added to the infected macrophage monolayers 24 h post infection. The Mtb load was calculated by qPCR based method after 2 days of co-culture with T lymphocytes (3 days post infection). The dotted line indicates the Mtb load in untreated cells at day 2 post infection.

J. Inhibition of Myc and lipid peroxidation improves control of Mtb by B6.Sst1S macrophages co-cultured with immune T cells isolated from BCG-vaccinated B6 mice. BMDMs were pretreated with 10 ng/mL TNF alone or in combination with either Ferrostatin 1 (3 μM) or 10058-F4 (10 μM) for 16 h and subsequently infected with Mtb at MOI 1. At 24 h post infection the lymphocytes from BCG immunized B6 mice were

added to the infected macrophage monolayers. The Mtb loads were determined by qPCR based method after 2 days of co-culture with T cells (3 days post infection).

K. Effect of post-exposure BCG vaccination of the survival of Mtb infected B6.Sst1S mice. Mice were infected with Mtb for 2 months and subsequently vaccinated with BCG. The survival cures of vaccinated and non-vaccinated mice were compared using the Log-rank (Mantel-Cox) to determine statistical significance.

The data represent the means ± SD of three samples per experiment, representative of three independent experiments.

The statistical significance was performed by two-way ANOVA using Bonferroni's multiple comparison test (Panel B, H and I) and Tukey's multiple comparison test (Panel D-G). Significant differences are indicated with asterisks (*, $P < 0.05$; **, $P < 0.01$; ***, $P < 0.001$; ****, $P < 0.0001$).

Figure 7. Accumulation of lipid peroxidation products and stress escalation in macrophages during pulmonary TB progression.

A. 3D confocal image of B6.Sst1S,ifnβ-YFP mouse lung lesion stained with anti-4HNE antibody showing 4HNE+ (magenta) cells expressing YFP (green). Mtb reporter Mtb (smyc' :: mCherry) is red. Lower image – individual images of 4HNE+ cells expressing YFP (2D).

B. 3D confocal image of B6.Sst1S,ifnβ-YFP mouse lung lesion stained with Iba1- and iNOS-specific antibodies: YFP (green), Iba1+ (magenta), iNOS+ (teal) and reporter Mtb (smyc' :: mCherry) in red. Upper image - 3D, Lower image – individual images of Iba1+ and iNOS+ cells expressing YFP (2D).

C. Heatmap of interferon inducible genes differentially expressed in Iba1+ cells within multibacillary vs paucibacillary lesions (fold change 1.5 and above). Pooled gene list of IFN type I and II regulated genes was assembled using public databases (as described in Methods).

D. fmIHC images of B6.Sst1S, ifnβ-YFP mouse lung lesions. Paucibacillary (P) and multibacillary (M) lesions were stained with phospho-c-JUN- (magenta), Chac1-(yellow), iNOS- (teal), Iba1- (red) and YFP- (green) specific antibodies.

E. The accumulation of macrophages co-expressing activation and stress markers during the disease progression. Paucibacillary (n=12) and multibacillary (n=12) lung lesions of B6.Sst1S, ifnβ-YFP mice were compared using area quantification of double positive iNOS+ phospho-cJUN+, iNOS+Chac1+, YFP+ phospho-cJUN+, and YFP+Chac1+ marker combinations.

The data represent the means ± SD and the statistical significance was performed by unpaired t-test (Panels E). Significant differences are indicated with asterisks (*, $P < 0.05$; **, $P < 0.01$; ***, $P < 0.001$; ****, $P < 0.0001$).

Figure 8. Schematic representation of TNF responses to in B6 and B6.Sst1S macrophages.

B6 and B6.Sst1S:

1. TNF activates c-Myc expression (Fig.1E, G and H and Fig.5A and B).

2. TNF induces Ifnβ expression.

3. TNF stimulation leads to NRF2 upregulation (Fig.2A-E).

In B6:

4. Ifnβ induces Sp110 and Sp140 that co-activate NRF2 and suppress c-Myc, respectively.

5. NRF2 activates antioxidant defense (AOD) that inhibits lipid peroxidation (LPO) (Fig.2A-G, 2J, Suppl. Fig.2A-C).

In B6.Sst1S:

6. Sp110 and Sp140 are not expressed.

7. Myc is upregulated (Fig.5A and B, Suppl. Fig.1B, D) and inhibits ferritin increasing labile iron pool and co-stimulated IFNβ (Fig.5C-H).

8. Deficient AOD activation coupled with increased labile iron pool promotes accumulation of LPO products (Fig.3A-H, Suppl. Fig.3C-G).

9. LPO co-stimulates IFNβ leading to superinduction (Fig.4F and G, Suppl. Fig.3H and I).

10. IFN-I activates ISR and induces Chac1 that further inhibits the AOD and increases LPO (Fig.3I, Suppl. Fig.3B).

11. Alternative mechanisms of IFN-mediated dysregulation of AOD defense and iron homeostasis.

References

1. M. Orgeur, R. Brosch, Evolution of virulence in the Mycobacterium tuberculosis complex. *Curr. Opin. Microbiol.* **41**, 68-75 (2018).
2. WHO, Global Health TB Report. *https://www.who.int/tb/publications/global_report/en/*, (2022).
3. A. J. Pagan, L. Ramakrishnan, The Formation and Function of Granulomas. *Annu Rev Immunol* **36**, 639-665 (2018).
4. M. Pai *et al.*, Tuberculosis. *Nat Rev Dis Primers* **2**, 16076 (2016).
5. C. R. Horsburgh, Jr., E. J. Rubin, Clinical practice. Latent tuberculosis infection in the United States. *N Engl J Med* **364**, 1441-1448 (2011).
6. M. R. Reichler *et al.*, Risk and Timing of Tuberculosis Among Close Contacts of Persons with Infectious Tuberculosis. *J Infect Dis* **218**, 1000-1008 (2018).
7. P. K. Drain *et al.*, Incipient and Subclinical Tuberculosis: a Clinical Review of Early Stages and Progression of Infection. *Clin Microbiol Rev* **31**, (2018).
8. M. A. Behr, E. Kaufmann, J. Duffin, P. H. Edelstein, L. Ramakrishnan, Latent Tuberculosis: Two Centuries of Confusion. *Am J Resp Crit Care* **204**, 142-148 (2021).
9. J. D. Simmons *et al.*, Immunological mechanisms of human resistance to persistent Mycobacterium tuberculosis infection. *Nature Reviews Immunology* **282**, 677 (2018).
10. S. B. Cohen, B. H. Gern, K. B. Urdahl, The Tuberculous Granuloma and Preexisting Immunity. *Annual Review of Immunology* **40**, 589-614 (2022).
11. T. Ulrichs *et al.*, Modified immunohistological staining allows detection of Ziehl–Neelsen□negative Mycobacterium tuberculosis organisms and their precise localization in human tissue. (2005).
12. C. Bussi, M. G. Gutierrez, Mycobacterium tuberculosis infection of host cells in space and time. *FEMS Microbiol Rev* **43**, 341-361 (2019).
13. A. O'Garra *et al.*, The immune response in tuberculosis. *Annu Rev Immunol* **31**, 475-527 (2013).
14. J. D. Ernst, Mechanisms of M. tuberculosis Immune Evasion as Challenges to TB Vaccine Design. *Cell host & microbe* **24**, 34-42 (2018).
15. P. Ogongo, J. D. Ernst, Finding antigens for TB vaccines: the good, the bad and the useless. *Nat Med* **29**, 35-36 (2023).
16. A. R. DiNardo *et al.*, Tuberculosis Endotypes to Guide Stratified Host-Directed Therapy. *Med* **2**, 217-232 (2021).
17. A. Apt, I. Kramnik, Man and mouse TB: contradictions and solutions. *Tuberculosis (Edinburgh, Scotland)* **89**, 195 - 198 (2009).
18. R. J. North, Y.-J. Jung, Immunity to Tuberculosis. *Immunology* **22**, 599-623 (2004).
19. I. Kramnik, G. Beamer, Mouse models of human TB pathology: roles in the analysis of necrosis and the development of host-directed therapies. *Semin Immunopathol* **38**, 221-237 (2016).
20. I. Kramnik, P. Demant, B. B. Bloom, Susceptibility to tuberculosis as a complex genetic trait: analysis using recombinant congenic strains of mice. *Novartis Found Symp* **217**, 120-131; discussion 132-127 (1998).

21. I. Kramnik, W. F. Dietrich, P. Demant, B. R. Bloom, Genetic control of resistance to experimental infection with virulent Mycobacterium tuberculosis. *Proc Natl Acad Sci U S A* **97**, 8560-8565 (2000).
22. B. S. Yan, A. Kirby, Y. V. Shebzukhov, M. J. Daly, I. Kramnik, Genetic architecture of tuberculosis resistance in a mouse model of infection. *Genes Immun* **7**, 201-210 (2006).
23. J. Sissons *et al.*, Multigenic control of tuberculosis resistance: analysis of a QTL on mouse chromosome 7 and its synergism with sst1. *Genes Immun* **10**, 37-46 (2009).
24. H. Pan *et al.*, Ipr1 gene mediates innate immunity to tuberculosis. *Nature* **434**, 767-772 (2005).
25. A. V. Pichugin, B. S. Yan, A. Sloutsky, L. Kobzik, I. Kramnik, Dominant role of the sst1 locus in pathogenesis of necrotizing lung granulomas during chronic tuberculosis infection and reactivation in genetically resistant hosts. *Am J Pathol* **174**, 2190-2201 (2009).
26. S. M. Yabaji *et al.*, Aberrant macrophage activation and failed regeneration of pulmonary epithelium promote tuberculosis progression uniquely in lung tissue. 2023.2010.2017.562695 (2023).
27. V. Boyartchuk *et al.*, The host resistance locus sst1 controls innate immunity to Listeria monocytogenes infection in immunodeficient mice. *J Immunol* **173**, 5112-5120 (2004).
28. B. S. Yan *et al.*, Progression of pulmonary tuberculosis and efficiency of bacillus Calmette-Guerin vaccination are genetically controlled via a common sst1-mediated mechanism of innate immunity. *J Immunol* **179**, 6919-6932 (2007).
29. X. He *et al.*, The sst1 resistance locus regulates evasion of type I interferon signaling by Chlamydia pneumoniae as a disease tolerance mechanism. *PLoS Pathog* **9**, e1003569 (2013).
30. B. Bhattacharya *et al.*, The integrated stress response mediates necrosis in murine Mycobacterium tuberculosis granulomas. *J Clin Invest* **131**, (2021).
31. D. X. Ji *et al.*, Type I interferon-driven susceptibility to Mycobacterium tuberculosis is mediated by IL-1Ra. *Nat Microbiol* **4**, 2128-2135 (2019).
32. L. Moreira-Teixeira, K. Mayer-Barber, A. Sher, A. O'Garra, Type I interferons in tuberculosis: Foe and occasionally friend. *J Exp Med* **215**, 1273-1285 (2018).
33. M. L. Donovan, T. E. Schultz, T. J. Duke, A. Blumenthal, Type I Interferons in the Pathogenesis of Tuberculosis: Molecular Drivers and Immunological Consequences. *Front Immunol* **8**, 1633 (2017).
34. S. A. Stanley, J. E. Johndrow, P. Manzanillo, J. S. Cox, The Type I IFN response to infection with Mycobacterium tuberculosis requires ESX-1-mediated secretion and contributes to pathogenesis. *J Immunol* **178**, 3143-3152 (2007).
35. D. I. Kotov *et al.*, Early cellular mechanisms of type I interferon-driven susceptibility to tuberculosis. *Cell*, (2023).
36. D. X. Ji *et al.*, Role of the transcriptional regulator SP140 in resistance to bacterial infections via repression of type I interferons. *Elife* **10**, (2021).
37. I. Fraschilla, K. L. Jeffrey, The Speckled Protein (SP) Family: Immunity's Chromatin Readers. *Trends Immunol* **41**, 572-585 (2020).
38. M. N. Lee *et al.*, Identification of regulators of the innate immune response to cytosolic DNA and retroviral infection by an integrative approach. *Nature Immunology* **14**, 179 - 185 (2012).

39. F. Matesanz *et al.*, A functional variant that affects exon-skipping and protein expression of SP140as genetic mechanism predisposing to multiple sclerosis. *Human molecular genetics* **24**, 5619 - 5627 (2015).
40. S. Mehta *et al.*, Maintenance of macrophage transcriptional programs and intestinal homeostasis by epigenetic reader SP140. *Sci Immunol* **2**, (2017).
41. H. Amatullah *et al.*, Epigenetic reader SP140 loss of function drives Crohn's disease due to uncontrolled macrophage topoisomerases. *Cell* **185**, 3232-3247.e3218 (2022).
42. H. Kamata *et al.*, Reactive Oxygen Species Promote TNFα-Induced Death and Sustained JNK Activation by Inhibiting MAP Kinase Phosphatases. *Cell* **120**, 649 - 661 (2005).
43. H. Blaser, C. Dostert, T. W. Mak, D. Brenner, TNF and ROS Crosstalk in Inflammation. *Trends Cell Biol.* **26**, 249-261 (2016).
44. L. Boccuni *et al.*, Stress signaling boosts interferon-induced gene transcription in macrophages. *Sci. Signal.* **15**, eabq5389 (2022).
45. M. Karin, E. Gallagher, From JNK to Pay Dirt: Jun Kinases, their Biochemistry, Physiology and Clinical Importance. *IUBMB Life* **57**, 283-295 (2005).
46. I. A. Buskiewicz *et al.*, Reactive oxygen species induce virus-independent MAVS oligomerization in systemic lupus erythematosus. *Sci. Signal.* **9**, ra115 - ra115 (2016).
47. M. Riedelberger *et al.*, Type I Interferon Response Dysregulates Host Iron Homeostasis and Enhances Candida glabrata Infection. *Cell host & microbe* **27**, 454 - 466.e458 (2020).
48. Y. Lei *et al.*, Elevated type I interferon responses potentiate metabolic dysfunction, inflammation, and accelerated aging in mtDNA mutator mice. (2021).
49. D. Zimmerli *et al.*, MYC promotes immune-suppression in triple-negative breast cancer via inhibition of interferon signaling. *Nature Communications* **13**, 6579 (2022).
50. S. Levy, H. J. Forman, C□Myc is a Nrf2□interacting protein that negatively regulates phase II genes through their electrophile responsive elements. *IUBMB Life* **62**, 237-246 (2010).
51. F. M. Torti, S. V. Torti, Regulation of ferritin genes and protein. *Blood* **99**, 3505 - 3516 (2002).
52. J. L. Flynn, J. Chan, Immune cell interactions in tuberculosis. *Cell* **185**, 4682-4702 (2022).
53. V. A. Huynh-Thu, P. Geurts, dynGENIE3: dynamical GENIE3 for the inference of gene networks from time series expression data. *Sci Rep* **8**, 3384 (2018).
54. E. Clough, T. Barrett, The Gene Expression Omnibus Database. *Methods Mol Biol* **1418**, 93-110 (2016).
55. V. Zhernovkov *et al.*, An Integrative Computational Approach for a Prioritization of Key Transcription Regulators Associated With Nanomaterial-Induced Toxicity. *Toxicol Sci* **171**, 303-314 (2019).
56. V. A. Huynh-Thu, A. Irrthum, L. Wehenkel, P. Geurts, Inferring regulatory networks from expression data using tree-based methods. *PLoS One* **5**, (2010).
57. B. R. Stockwell *et al.*, Ferroptosis: A Regulated Cell Death Nexus Linking Metabolism, Redox Biology, and Disease. *Cell* **171**, 273-285 (2017).
58. Q. Ma *et al.*, A mosquito small RNA genomics resource reveals dynamic evolution and host responses to viruses and transposons. *Genome Res* **31**, 512-528 (2021).
59. R. Jayewickreme *et al.*, Endogenous Retroviruses Provide Protection Against Vaginal HSV-2 Disease. *Front Immunol* **12**, 758721 (2021).

60. S. Scheu, P. Dresing, R. M. Locksley, Visualization of IFNbeta production by plasmacytoid versus conventional dendritic cells under specific stimulation conditions in vivo. *Proc Natl Acad Sci U S A* **105**, 20416-20421 (2008).
61. R. C. Lavin, S. Tan, Spatial relationships of intra-lesion heterogeneity in Mycobacterium tuberculosis microenvironment, replication status, and drug efficacy. *PLoS Pathog* **18**, e1010459 (2022).
62. C. R. Merritt *et al.*, Multiplex digital spatial profiling of proteins and RNA in fixed tissue. *Nat Biotechnol* **38**, 586-599 (2020).
63. M. L. DeDiego, L. Martinez-Sobrido, D. J. Topham, Novel Functions of IFI44L as a Feedback Regulator of Host Antiviral Responses. *J. Virol.* **93**, (2019).
64. H. Jiang, L. Tsang, H. Wang, C. Liu, IFI44L as a Forward Regulator Enhancing Host Antituberculosis Responses. *J. Immunol. Res.* **2021**, 1-12 (2021).
65. E. P. Amaral *et al.*, BACH1 promotes tissue necrosis and Mycobacterium tuberculosis susceptibility. *Nat Microbiol*, (2023).
66. M. S. Mortensen, J. Ruiz, J. L. Watts, Polyunsaturated Fatty Acids Drive Lipid Peroxidation during Ferroptosis. *Cells* **12**, (2023).
67. Leonard D. Goldstein *et al.*, Recurrent Loss of NFE2L2 Exon 2 Is a Mechanism for Nrf2 Pathway Activation in Human Cancers. *Cell Rep.* **16**, 2605-2617 (2016).
68. C. Tonelli, I. I. C. Chio, D. a. Tuveson, Transcriptional Regulation by Nrf2. *Antioxidants & Redox Signaling* **29**, 1727 - 1745 (2018).
69. W. Li *et al.*, An internal ribosomal entry site mediates redox-sensitive translation of Nrf2. *Nucleic Acids Res.* **38**, 778-788 (2010).
70. K. P. Shay, A. J. Michels, W. Li, A.-N. T. Kong, T. M. Hagen, Cap-independent Nrf2 translation is part of a lipoic acid-stimulated detoxification stress response. *Biochim. Biophys. Acta (BBA) - Mol. Cell Res.* **1823**, 1102-1109 (2012).
71. Z. Shi, M. Barna, Translating the Genome in Time and Space: Specialized Ribosomes, RNA Regulons, and RNA-Binding Proteins. *Annual review of cell and developmental biology* **31**, 31 - 54 (2015).
72. A. Basu *et al.*, Requirement of rRNA methylation for 80S ribosome assembly on a cohort of cellular internal ribosome entry sites. *Molecular and Cellular Biology* **31**, 4482 - 4499 (2011).
73. B. Mazumder *et al.*, Regulated Release of L13a from the 60S Ribosomal Subunit as A Mechanism of Transcript-Specific Translational Control 9500 Euclid Avenue 2121 Euclid Avenue. *Cell* **115**, 187 - 198 (2003).
74. A. Basu *et al.*, Ribosomal Protein L13a Deficiency in Macrophages Promotes Atherosclerosis by Limiting Translation Control-Dependent Retardation of Inflammation. *Arteriosclerosis, Thrombosis, and Vascular Biology* **34**, 533 - 542 (2014).
75. D. Poddar *et al.*, An Extraribosomal Function of Ribosomal Protein L13a in Macrophages Resolves Inflammation. *Journal of immunology (Baltimore, Md. : 1950)* **190**, 3600 - 3612 (2013).
76. D. Poddar, R. Kaur, W. M. Baldwin, B. Mazumder, L13a-dependent translational control in macrophages limits the pathogenesis of colitis. *Cellular and Molecular Immunology*, (2015).
77. T. T. Susanto *et al.*, RAPIDASH: A tag-free enrichment of ribosome-associated proteins reveals compositional dynamics in embryonic tissues and stimulated macrophages. *bioRxiv*, 2023.2012.2007.570613 (2023).

78. I. R. Fraschilla, K. L. Jeffrey, Speckled Protein (SP)140, an immune-specific chromatin reader, contains a CARD and chromatin-interacting domains that dictate subnuclear localization and macrophage identity. *The Journal of Immunology* **204**, 69.27 - 69.27 (2020).
79. K. J. Wu, A. Polack, R. Dalla-Favera, Coordinated regulation of iron-controlling genes, H-ferritin and IRP2, by c-MYC. *Science (New York, NY)* **283**, 676 - 679 (1999).
80. D. Pisu, L. Huang, J. K. Grenier, D. G. Russell, Dual RNA-Seq of Mtb-Infected Macrophages In Vivo Reveals Ontologically Distinct Host-Pathogen Interactions. *Cell Rep* **30**, 335-350 e334 (2020).
81. R. R. Crawford *et al.*, Human CHAC1 Protein Degrades Glutathione, and mRNA Induction Is Regulated by the Transcription Factors ATF4 and ATF3 and a Bipartite ATF/CRE Regulatory Element. *The Journal of biological chemistry* **290**, 15878 - 15891 (2015).
82. A. C. Rothchild *et al.*, Alveolar macrophages generate a noncanonical NRF2-driven transcriptional response to Mycobacterium tuberculosis in vivo. *Sci Immunol* **4**, (2019).
83. S. B. Berry *et al.*, Disruption of Aldehyde Dehydrogenase 2 protects against bacterial infection. *bioRxiv*, (2023).
84. E. P. Amaral *et al.*, A major role for ferroptosis in Mycobacterium tuberculosis-induced cell death and tissue necrosis. *J Exp Med* **216**, 556-570 (2019).
85. D. L. Piddington *et al.*, Cu,Zn superoxide dismutase of Mycobacterium tuberculosis contributes to survival in activated macrophages that are generating an oxidative burst. *Infect Immun* **69**, 4980-4987 (2001).
86. H. T. Pacl, V. P. Reddy, V. Saini, K. C. Chinta, A. J. C. Steyn, Host-pathogen redox dynamics modulate Mycobacterium tuberculosis pathogenesis. *Pathog Dis* **76**, (2018).
87. D. Mahamed *et al.*, Intracellular growth of Mycobacterium tuberculosis after macrophage cell death leads to serial killing of host cells. *eLife* **6**, 5210 (2017).
88. V. Gorbunova *et al.*, Cancer resistance in the blind mole rat is mediated by concerted necrotic cell death mechanism. *Proceedings of the National Academy of Sciences of the United States of America* **109**, 19392 - 19396 (2012).
89. K. I. Leonova *et al.*, p53 cooperates with DNA methylation and a suicidal interferon response to maintain epigenetic silencing of repeats and noncoding RNAs. *Proc. Natl. Acad. Sci.* **110**, E89-E98 (2013).
90. S. M. Yabaji, S. Chatterjee, E. Waligursky, A. Gimelbrant, I. Kramnik, Medium throughput protocol for genome-based quantification of intracellular mycobacterial loads and macrophage survival during in vitro infection. *STAR Protoc* **3**, 101241 (2022).
91. A. Dobin *et al.*, STAR: ultrafast universal RNA-seq aligner. *Bioinformatics* **29**, 15-21 (2013).
92. Y. Liao, G. K. Smyth, W. Shi, featureCounts: an efficient general purpose program for assigning sequence reads to genomic features. *Bioinformatics* **30**, 923-930 (2014).
93. M. I. Love, W. Huber, S. Anders, Moderated estimation of fold change and dispersion for RNA-seq data with DESeq2. *Genome Biol* **15**, 550 (2014).
94. D. Wu, G. K. Smyth, Camera: a competitive gene set test accounting for inter-gene correlation. *Nucleic Acids Res* **40**, e133 (2012).
95. A. Lachmann *et al.*, Massive mining of publicly available RNA-seq data from human and mouse. *Nat Commun* **9**, 1366 (2018).

96. H. Hu *et al.*, AnimalTFDB 3.0: a comprehensive resource for annotation and prediction of animal transcription factors. *Nucleic Acids Res* **47**, D33-D38 (2019).
97. M. J. Alvarez *et al.*, Functional characterization of somatic mutations in cancer using network-based inference of protein activity. *Nat Genet* **48**, 838-847 (2016).
98. P. Shannon *et al.*, Cytoscape: a software environment for integrated models of biomolecular interaction networks. *Genome Res* **13**, 2498-2504 (2003).
99. H. Imrichova, G. Hulselmans, Z. K. Atak, D. Potier, S. Aerts, i-cisTarget 2015 update: generalized cis-regulatory enrichment analysis in human, mouse and fly. *Nucleic Acids Res* **43**, W57-64 (2015).
100. R. Hong *et al.*, Comprehensive generation, visualization, and reporting of quality control metrics for single-cell RNA sequencing data. *Nat Commun* **13**, 1688 (2022).
101. S. Yang *et al.*, Decontamination of ambient RNA in single-cell RNA-seq with DecontX. *Genome Biol* **21**, 57 (2020).
102. T. Stuart *et al.*, Comprehensive Integration of Single-Cell Data. *Cell* **177**, 1888-1902 e1821 (2019).
103. K. Street *et al.*, Slingshot: cell lineage and pseudotime inference for single-cell transcriptomics. *BMC Genomics* **19**, 477 (2018).
104. V. Picard, S. Epsztejn, P. Santambrogio, Z. I. Cabantchik, C. Beaumont, Role of ferritin in the control of the labile iron pool in murine erythroleukemia cells. *J Biol Chem* **273**, 15382-15386 (1998).
105. F. Thomas *et al.*, Calcein as a fluorescent probe for ferric iron. Application to iron nutrition in plant cells. *J Biol Chem* **274**, 13375-13383 (1999).
106. G. Dayama, K. Bulekova, N. C. Lau, Extending and Running the Mosquito Small RNA Genomics Resource Pipeline. *Methods Mol Biol* **2509**, 341-352 (2022).
107. W. Bao, K. K. Kojima, O. Kohany, Repbase Update, a database of repetitive elements in eukaryotic genomes. *Mob DNA* **6**, 11 (2015).
108. P. Danaher *et al.*, Advances in mixed cell deconvolution enable quantification of cell types in spatial transcriptomic data. *Nat Commun* **13**, 385 (2022).
109. E. Y. Chen *et al.*, Enrichr: interactive and collaborative HTML5 gene list enrichment analysis tool. *BMC Bioinformatics* **14**, 128 (2013).
110. Z. Xie *et al.*, Gene Set Knowledge Discovery with Enrichr. *Curr Protoc* **1**, e90 (2021).
111. A. Liberzon *et al.*, The Molecular Signatures Database (MSigDB) hallmark gene set collection. *Cell Syst* **1**, 417-425 (2015).

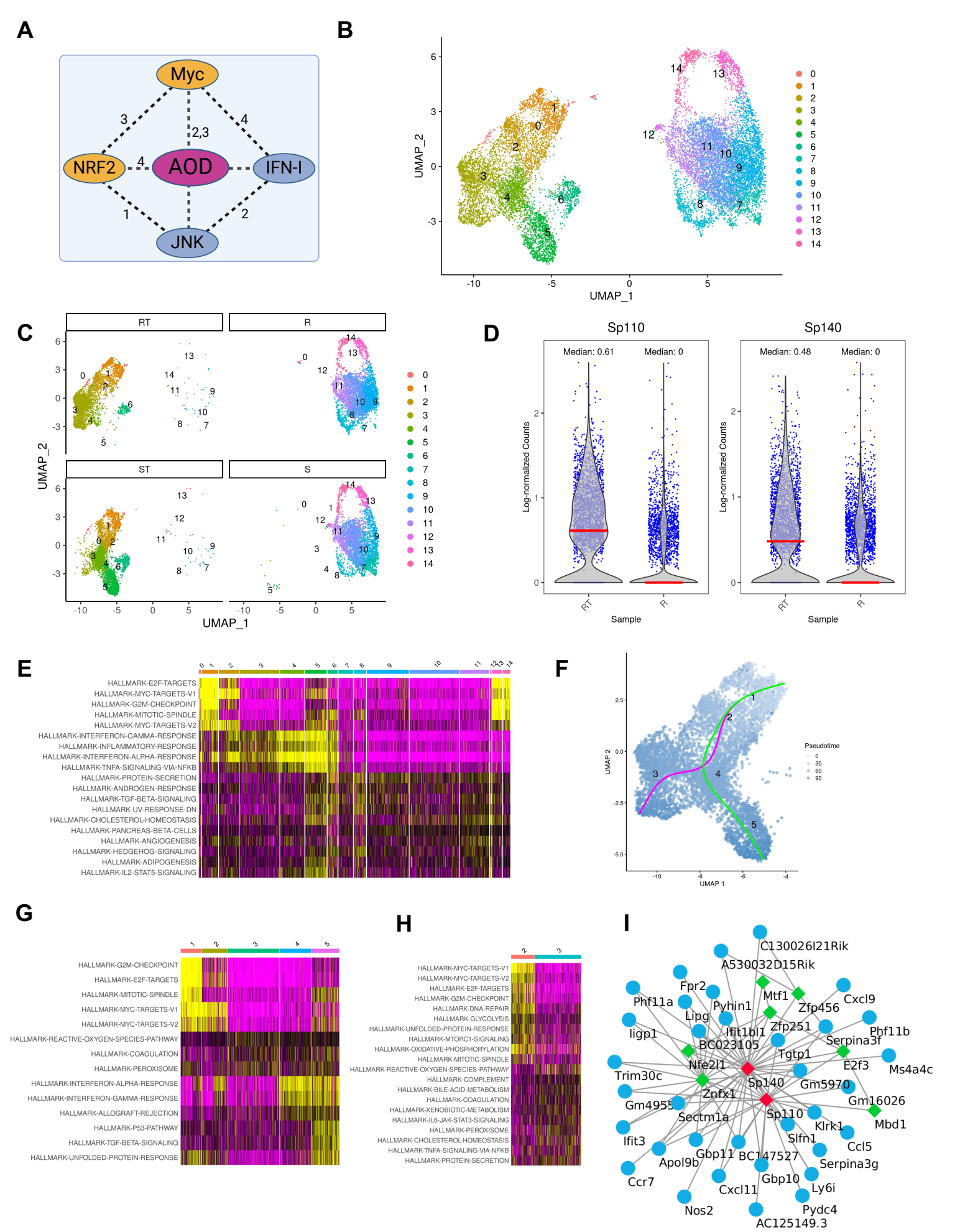
A
Myc
NRF2
AOD
IFN-I
JNK
3
2,3
4
4
1
2
B
UMAP_2
UMAP_1
C
RT
R
ST
S
UMAP_2
UMAP_1
D
Sp110
Sp140
Median: 0.61
Median: 0
Median: 0.48
Median: 0
Log-normalized Counts
Sample
E
HALLMARK-E2F-TARGETS
HALLMARK-MYC-TARGETS-V1
HALLMARK-G2M-CHECKPOINT
HALLMARK-MITOTIC-SPINDLE
HALLMARK-MYC-TARGETS-V2
HALLMARK-INTERFERON-GAMMA-RESPONSE
HALLMARK-INFLAMMATORY-RESPONSE
HALLMARK-INTERFERON-ALPHA-RESPONSE
HALLMARK-TNFA-SIGNALING-VIA-NFKB
HALLMARK-PROTEIN-SECRETION
HALLMARK-ANDROGEN-RESPONSE
HALLMARK-TGF-BETA-SIGNALING
HALLMARK-UV-RESPONSE-DN
HALLMARK-CHOLESTEROL-HOMEOSTASIS
HALLMARK-PANCREAS-BETA-CELLS
HALLMARK-ANGIOGENESIS
HALLMARK-HEDGEHOG-SIGNALING
HALLMARK-ADIPOGENESIS
HALLMARK-IL2-STAT5-SIGNALING
F
Pseudotime
UMAP 2
UMAP 1
G
HALLMARK-G2M-CHECKPOINT
HALLMARK-E2F-TARGETS
HALLMARK-MITOTIC-SPINDLE
HALLMARK-MYC-TARGETS-V1
HALLMARK-MYC-TARGETS-V2
HALLMARK-REACTIVE-OXYGEN-SPECIES-PATHWAY
HALLMARK-COAGULATION
HALLMARK-PEROXISOME
HALLMARK-INTERFERON-ALPHA-RESPONSE
HALLMARK-INTERFERON-GAMMA-RESPONSE
HALLMARK-ALLOGRAFT-REJECTION
HALLMARK-P53-PATHWAY
HALLMARK-TGF-BETA-SIGNALING
HALLMARK-UNFOLDED-PROTEIN-RESPONSE
H
HALLMARK-MYC-TARGETS-V1
HALLMARK-MYC-TARGETS-V2
HALLMARK-E2F-TARGETS
HALLMARK-G2M-CHECKPOINT
HALLMARK-DNA-REPAIR
HALLMARK-GLYCOLYSIS
HALLMARK-UNFOLDED-PROTEIN-RESPONSE
HALLMARK-MTORC1-SIGNALING
HALLMARK-OXIDATIVE-PHOSPHORYLATION
HALLMARK-MITOTIC-SPINDLE
HALLMARK-REACTIVE-OXYGEN-SPECIES-PATHWAY
HALLMARK-COMPLEMENT
HALLMARK-BILE-ACID-METABOLISM
HALLMARK-COAGULATION
HALLMARK-XENOBIOTIC-METABOLISM
HALLMARK-IL6-JAK-STAT3-SIGNALING
HALLMARK-PEROXISOME
HALLMARK-CHOLESTEROL-HOMEOSTASIS
HALLMARK-TNFA-SIGNALING-VIA-NFKB
HALLMARK-PROTEIN-SECRETION
I
C130026I21Rik
A530032D15Rik
Fpr2
Mtf1
Cxcl9
Phf11a
Pyhin1
Zfp456
Lipg
Ifit1bl1
Zfp251
Phf11b
Ifigp1
BC023105
Serpina3f
Tgtp1
Nfe2l1
E2f3
Ms4a4c
Trim30c
Sp140
Gm5970
Znfx1
Gm16026
Gm4955
Sp110
Sectm1a
Klrk1
Mbd1
Slfn1
Ifit3
Ccl5
Gbp11
BC147527
Apol9b
Serpina3g
Ccr7
Gbp10
Cxcl11
Ly6i
Nos2
Pydc4
AC125149.3

Figure 1

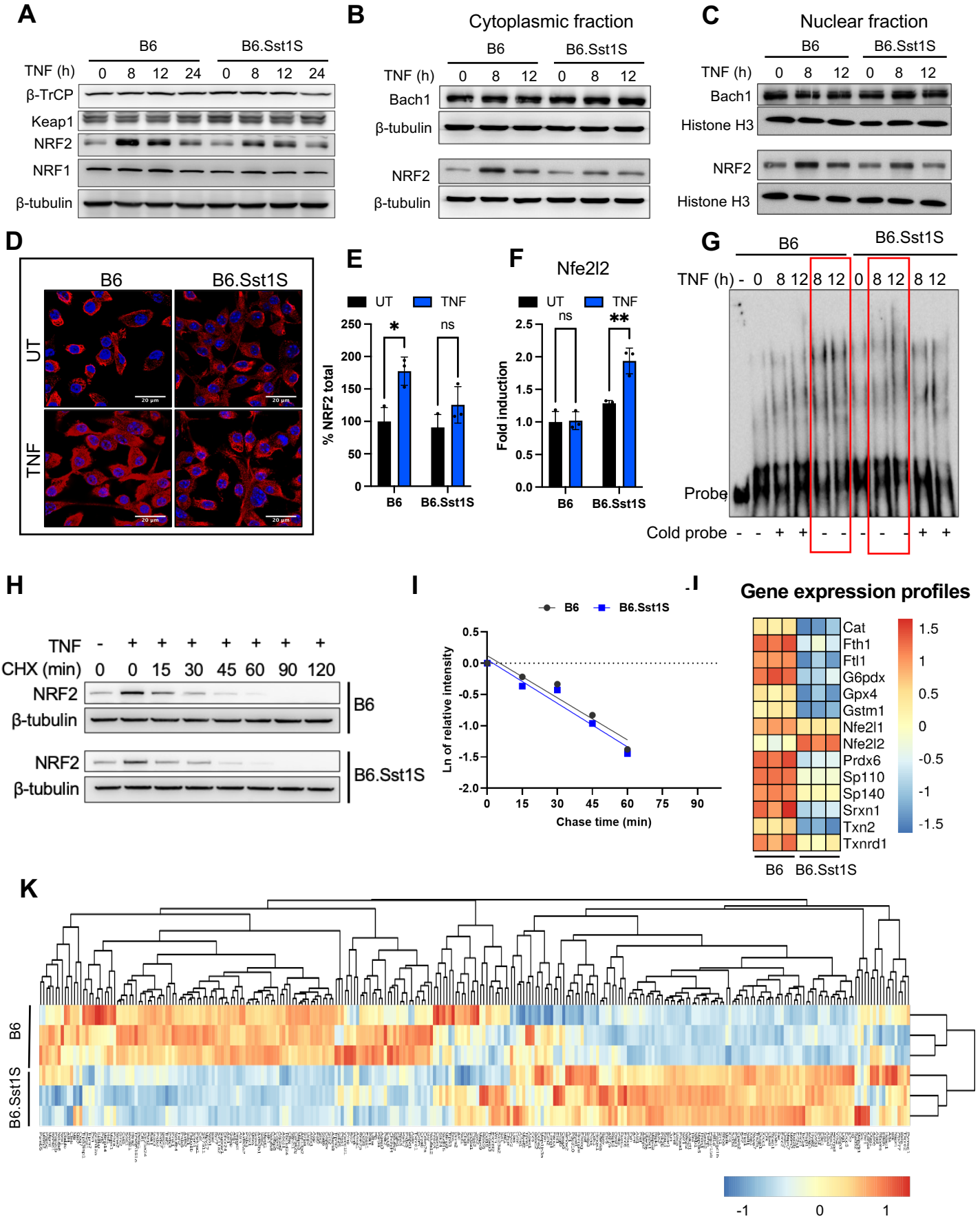
A
B6
B6.Sst1S
TNF (h)
0 8 12 24 0 8 12 24
β-TrCP
Keap1
NRF2
NRF1
β-tubulin
B
Cytoplasmic fraction
B6
B6.Sst1S
TNF (h)
0 8 12 0 8 12
Bach1
β-tubulin
NRF2
β-tubulin
C
Nuclear fraction
B6
B6.Sst1S
TNF (h)
0 8 12 0 8 12
Bach1
Histone H3
NRF2
Histone H3
D
B6
B6.Sst1S
UT
TNF
20 μm
E
UT
TNF
% NRF2 total
250
200
150
100
50
0
*
ns
B6
B6.Sst1S
F
Nfe2l2
UT
TNF
Fold induction
2.5
2.0
1.5
1.0
0.5
0.0
ns
**
B6
B6.Sst1S
G
B6
B6.Sst1S
TNF (h) - 0 8 12 8 12 0 8 12 8 12
Probe
Cold probe - - + + - - - - - + +
H
TNF - + + + + + + +
CHX (min) 0 0 15 30 45 60 90 120
NRF2
β-tubulin
B6
NRF2
β-tubulin
B6.Sst1S
I
B6
B6.Sst1S
Ln of relative intensity
0.5
0.0
-0.5
-1.0
-1.5
-2.0
0 15 30 45 60 75 90
Chase time (min)
J
Gene expression profiles
Cat
Fth1
Ftl1
G6pdx
Gpx4
Gstm1
Nfe2l1
Nfe2l2
Prdx6
Sp110
Sp140
Srxn1
Txn2
Txnrd1
1.5
1
0.5
0
-0.5
-1
-1.5
B6
B6.Sst1S
K
B6
B6.Sst1S
-1
0
1

Figure 2

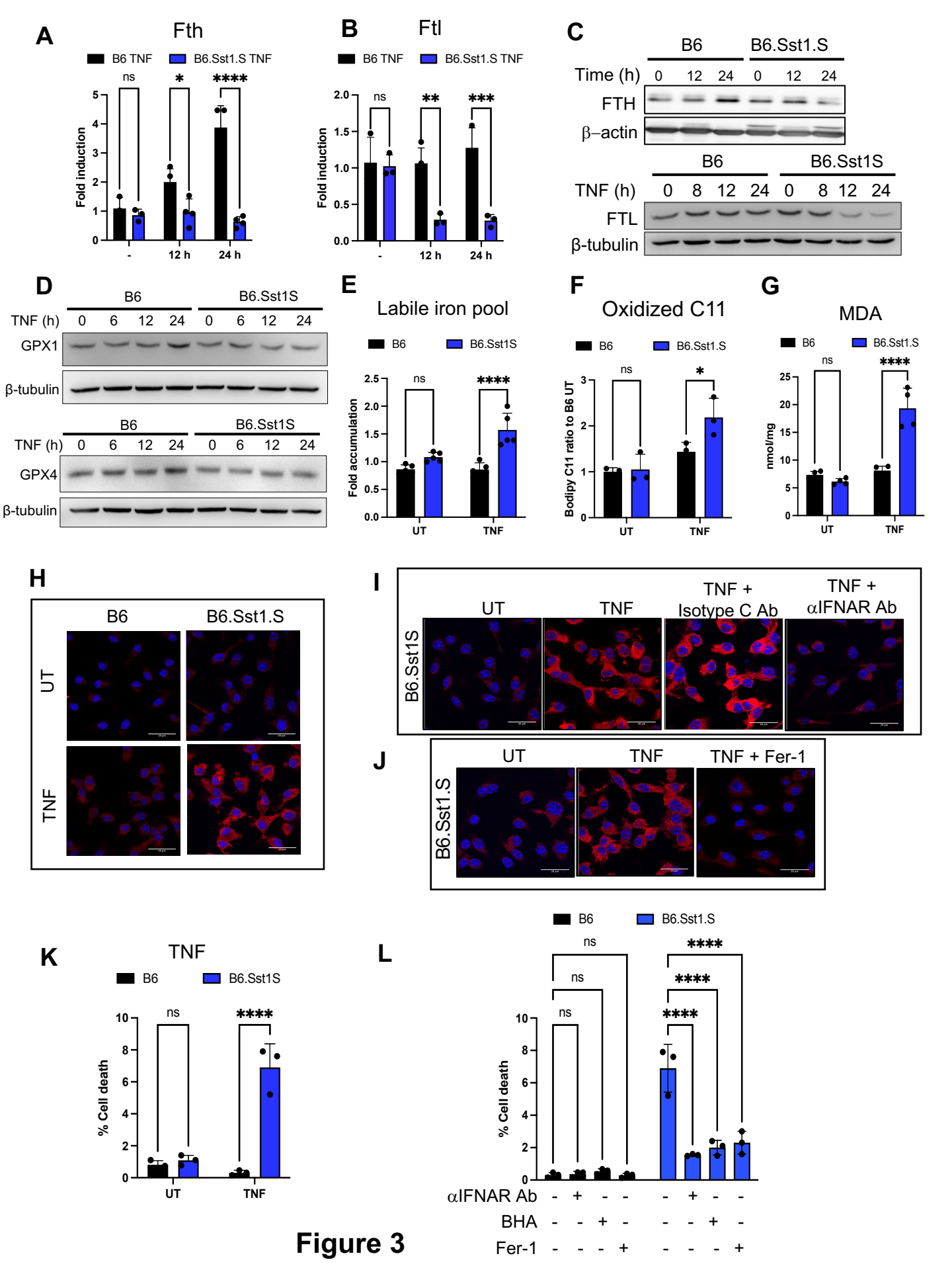
A
Fth
B6 TNF
B6.Sst1.S TNF
ns
*
****
Fold induction
-
12 h
24 h
B
Ftl
B6 TNF
B6.Sst1.S TNF
ns
**
***
Fold induction
-
12 h
24 h
C
B6
B6.Sst1.S
Time (h)
0 12 24 0 12 24
FTH
β–actin
B6
B6.Sst1S
TNF (h)
0 8 12 24 0 8 12 24
FTL
β-tubulin
D
B6
B6.Sst1S
TNF (h)
0 6 12 24 0 6 12 24
GPX1
β-tubulin
B6
B6.Sst1S
TNF (h)
0 6 12 24 0 6 12 24
GPX4
β-tubulin
E
Labile iron pool
B6
B6.Sst1S
ns
****
Fold accumulation
UT
TNF
F
Oxidized C11
B6
B6.Sst1.S
ns
*
Bodipy C11 ratio to B6 UT
UT
TNF
G
MDA
B6
B6.Sst1.S
ns
****
nmol/mg
UT
TNF
H
B6
B6.Sst1.S
UT
TNF
I
UT
TNF
TNF +
Isotype C Ab
TNF +
αIFNAR Ab
B6.Sst1S
J
UT
TNF
TNF + Fer-1
B6.Sst1.S
K
TNF
B6
B6.Sst1S
ns
****
% Cell death
UT
TNF
L
B6
B6.Sst1.S
ns
ns
ns
****
****
****
% Cell death
αIFNAR Ab - + - - - + - -
BHA - - + - - - + -
Fer-1 - - - + - - - +

Figure 3

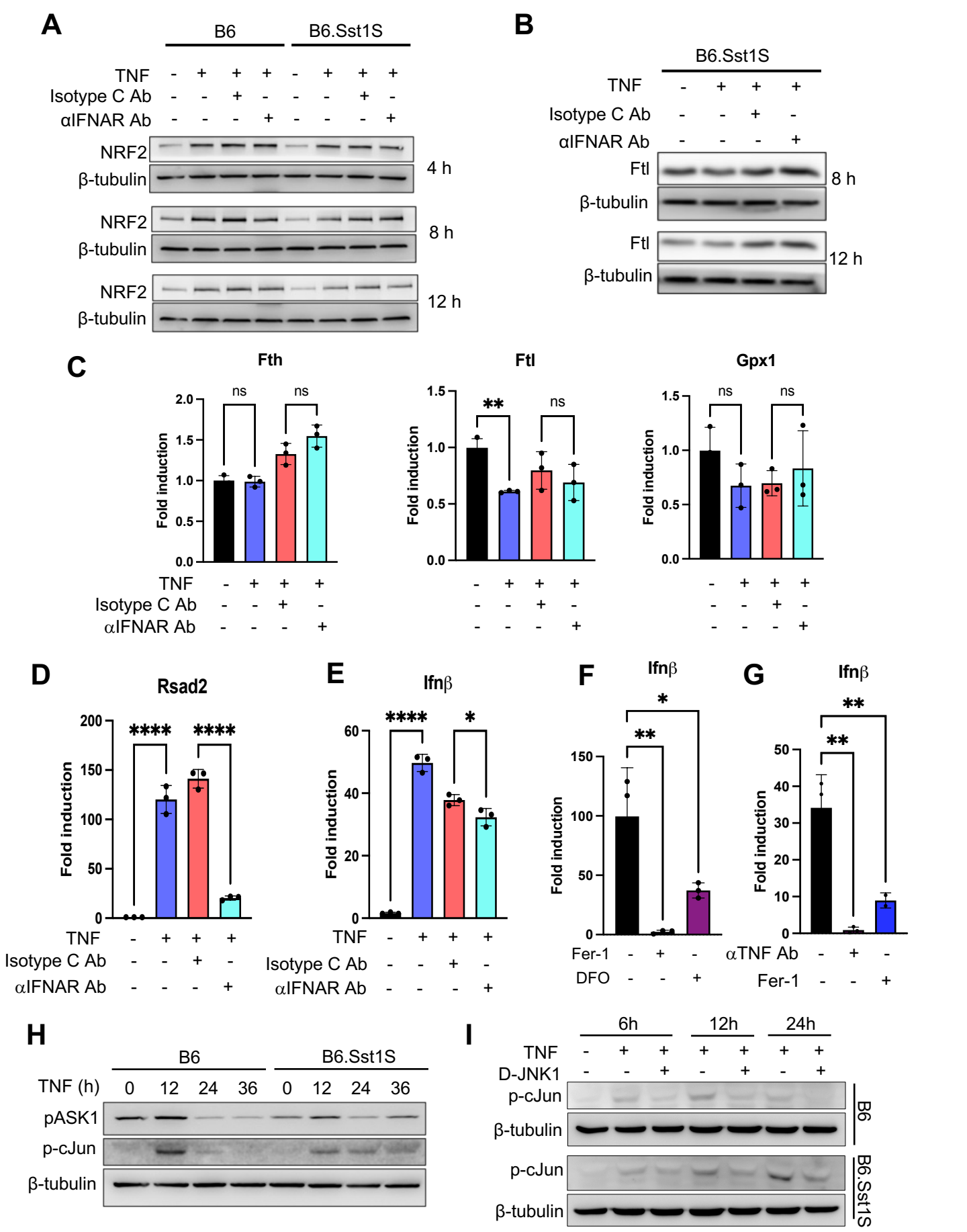
A
B6
B6.Sst1S
TNF
Isotype C Ab
αIFNAR Ab
NRF2
β-tubulin
4 h
8 h
12 h
B
B6.Sst1S
Ftl
C
Fth
Ftl
Gpx1
Fold induction
ns
**
D
Rsad2
****
E
Ifnβ
*
F
G
αTNF Ab
Fer-1
DFO
H
pASK1
p-cJun
TNF (h)
0
12
24
36
I
6h
12h
24h
D-JNK1
B6
B6.Sst1S

Figure 4

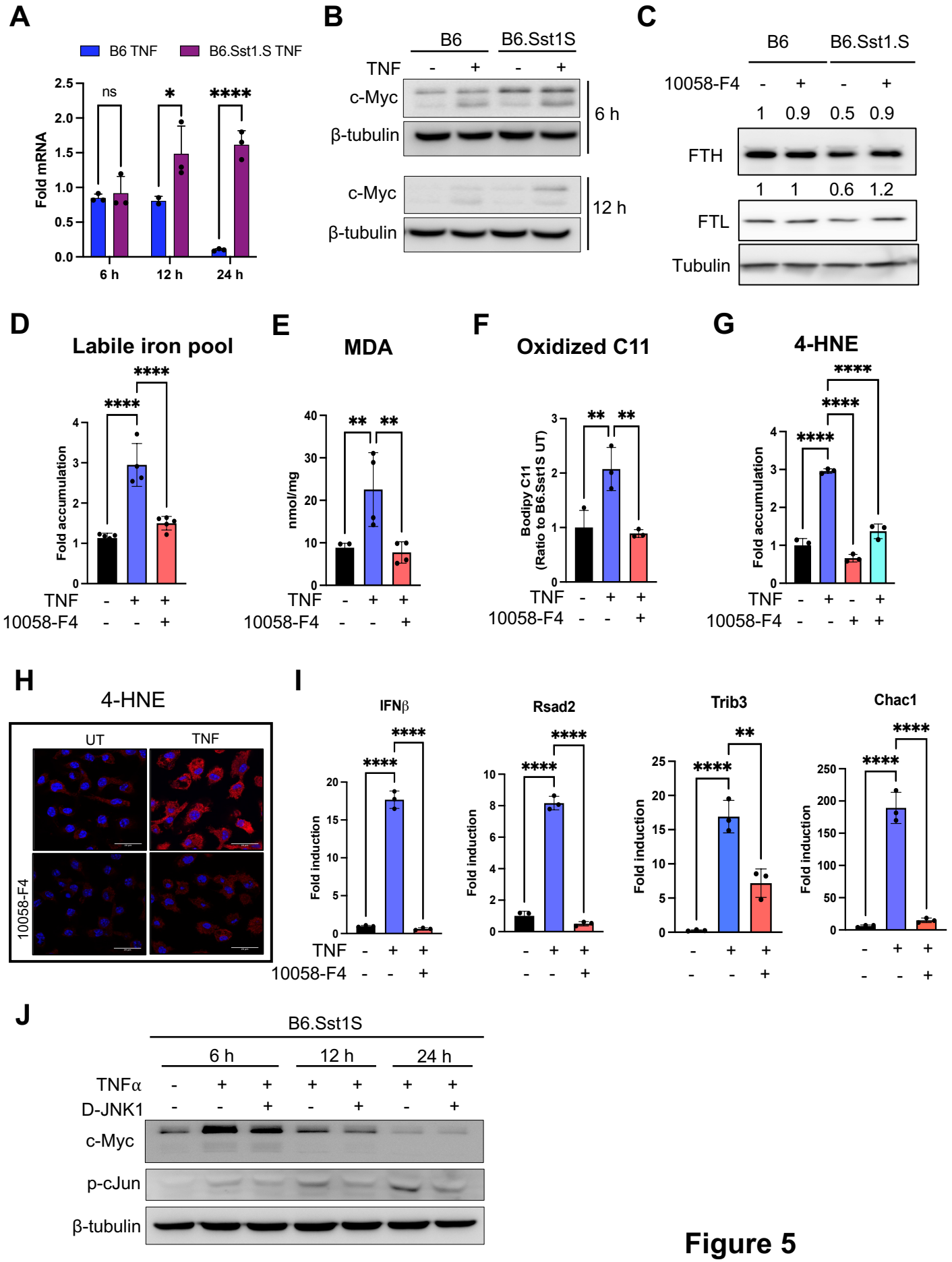
A
B6 TNF
B6.Sst1.S TNF
Fold mRNA
ns
*
****
6 h
12 h
24 h
B
B6
B6.Sst1S
TNF
c-Myc
β-tubulin
6 h
12 h
C
B6
B6.Sst1.S
10058-F4
1 0.9 0.5 0.9
FTH
1 1 0.6 1.2
FTL
Tubulin
D
Labile iron pool
Fold accumulation
E
MDA
nmol/mg
F
Oxidized C11
Bodipy C11 (Ratio to B6.Sst1S UT)
G
4-HNE
Fold accumulation
TNF
10058-F4
H
4-HNE
UT
TNF
10058-F4
I
IFNβ
Rsad2
Trib3
Chac1
Fold induction
J
B6.Sst1S
6 h
12 h
24 h
TNFα
D-JNK1
c-Myc
p-cJun
β-tubulin

Figure 5

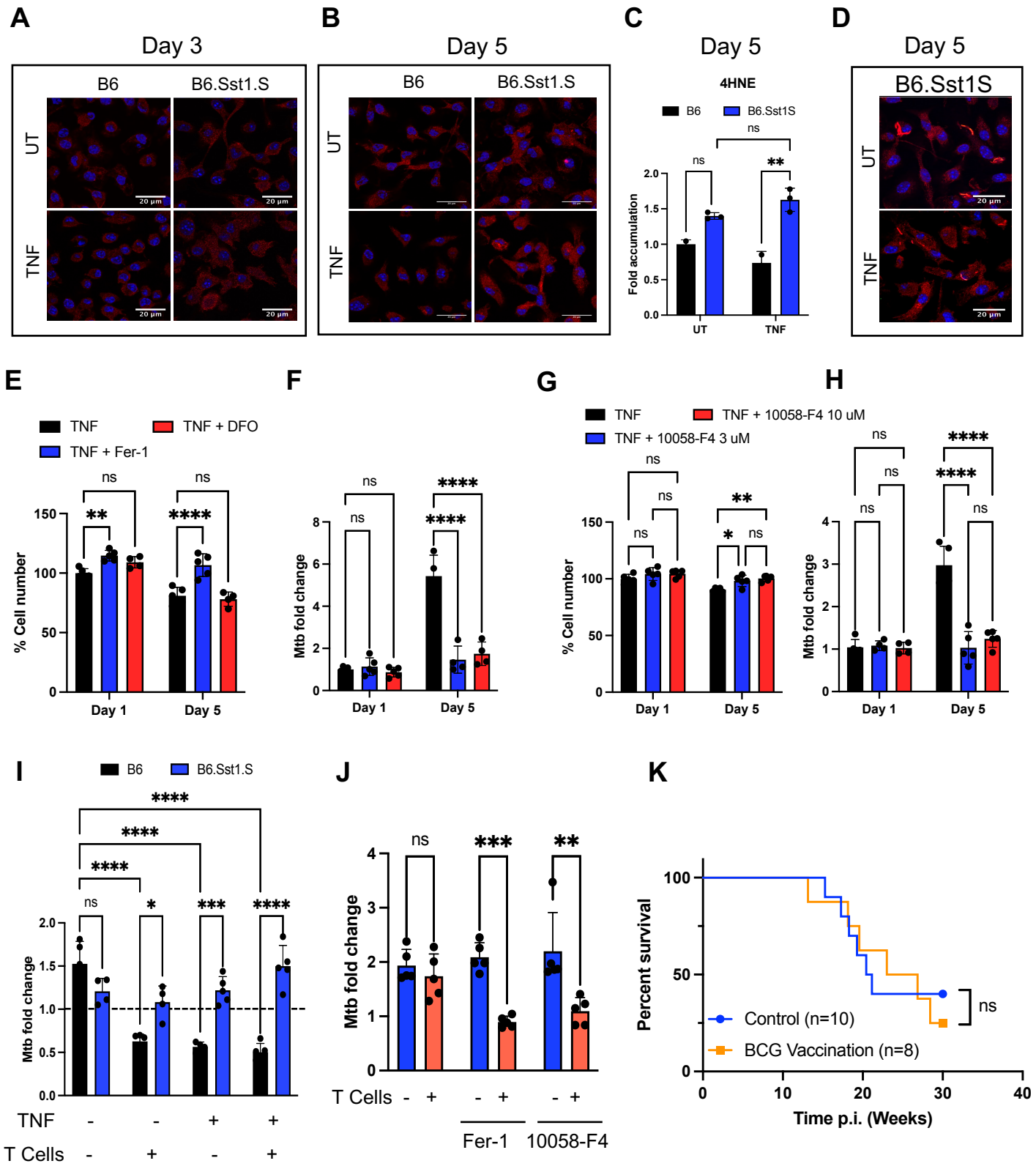
A
Day 3
B6
B6.Sst1.S
UT
TNF
20 µm
B
Day 5
B6
B6.Sst1.S
UT
TNF
C
Day 5
4HNE
B6
B6.Sst1S
ns
ns
**
Fold accumulation
2.0
1.5
1.0
0.5
0.0
UT
TNF
D
Day 5
B6.Sst1S
UT
TNF
20 µm
E
TNF
TNF + DFO
TNF + Fer-1
ns
ns
**
****
% Cell number
150
100
50
0
Day 1
Day 5
F
ns
ns
****
****
Mtb fold change
8
6
4
2
0
Day 1
Day 5
G
TNF
TNF + 10058-F4 10 uM
TNF + 10058-F4 3 uM
ns
ns
ns
**
*
ns
% Cell number
150
100
50
0
Day 1
Day 5
H
ns
ns
ns
****
****
ns
Mtb fold change
4
3
2
1
0
Day 1
Day 5
I
B6
B6.Sst1.S
****
****
****
ns
*
***
****
Mtb fold change
2.0
1.5
1.0
0.5
0.0
TNF - - + +
T Cells - + - +
J
ns
***
**
Mtb fold change
4
3
2
1
0
T Cells - + - + - +
Fer-1
10058-F4
K
Percent survival
100
50
0
Control (n=10)
BCG Vaccination (n=8)
ns
0
10
20
30
40
Time p.i. (Weeks)

Figure 6

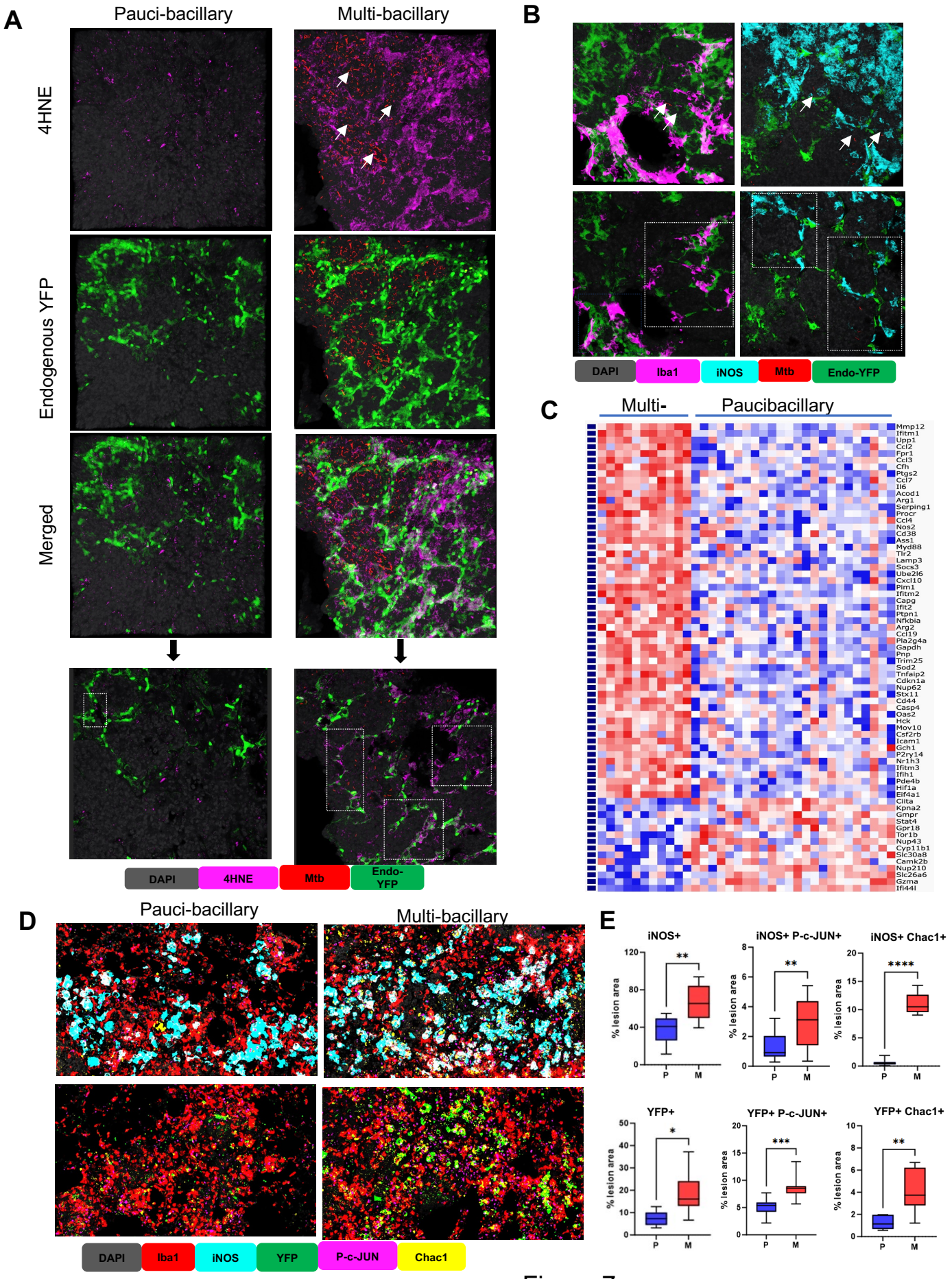
A
Pauci-bacillary
Multi-bacillary
4HNE
Endogenous YFP
Merged
DAPI
4HNE
Mtb
Endo-YFP
B
DAPI
Iba1
iNOS
Mtb
Endo-YFP
C
Multi-
Paucibacillary
Mmp12
Ifitm1
Upp1
Ccl2
Fpr1
Ccl3
Cfh
Ptgs2
Ccl7
Il6
Acod1
Arg1
Serping1
Procr
Ccl4
Nos2
Cd38
Ass1
Myd88
Tlr2
Lamp3
Socs3
Ube2l6
Cxcl10
Pim1
Ifitm2
Capg
Ifit2
Ptpn1
Nfkbia
Arg2
Ccl19
Pla2g4a
Gapdh
Pnp
Trim25
Sod2
Tnfaip2
Cdkn1a
Nup62
Stx11
Cd44
Casp4
Oas2
Hck
Mov10
Csf2rb
Icam1
Gch1
P2ry14
Nr1h3
Ifitm3
Ifih1
Pde4b
Hif1a
Eif4a1
Ciita
Kpna2
Gmpr
Stat4
Gpr18
Tor1b
Nup43
Cyp11b1
Slc30a8
Camk2b
Nup210
Slc26a6
Gzma
Ifi44l
D
Pauci-bacillary
Multi-bacillary
DAPI
Iba1
iNOS
YFP
P-c-JUN
Chac1
E
iNOS+
iNOS+ P-c-JUN+
iNOS+ Chac1+
YFP+
YFP+ P-c-JUN+
YFP+ Chac1+
% lesion area
P
M
**
****
*
***

Figure 7

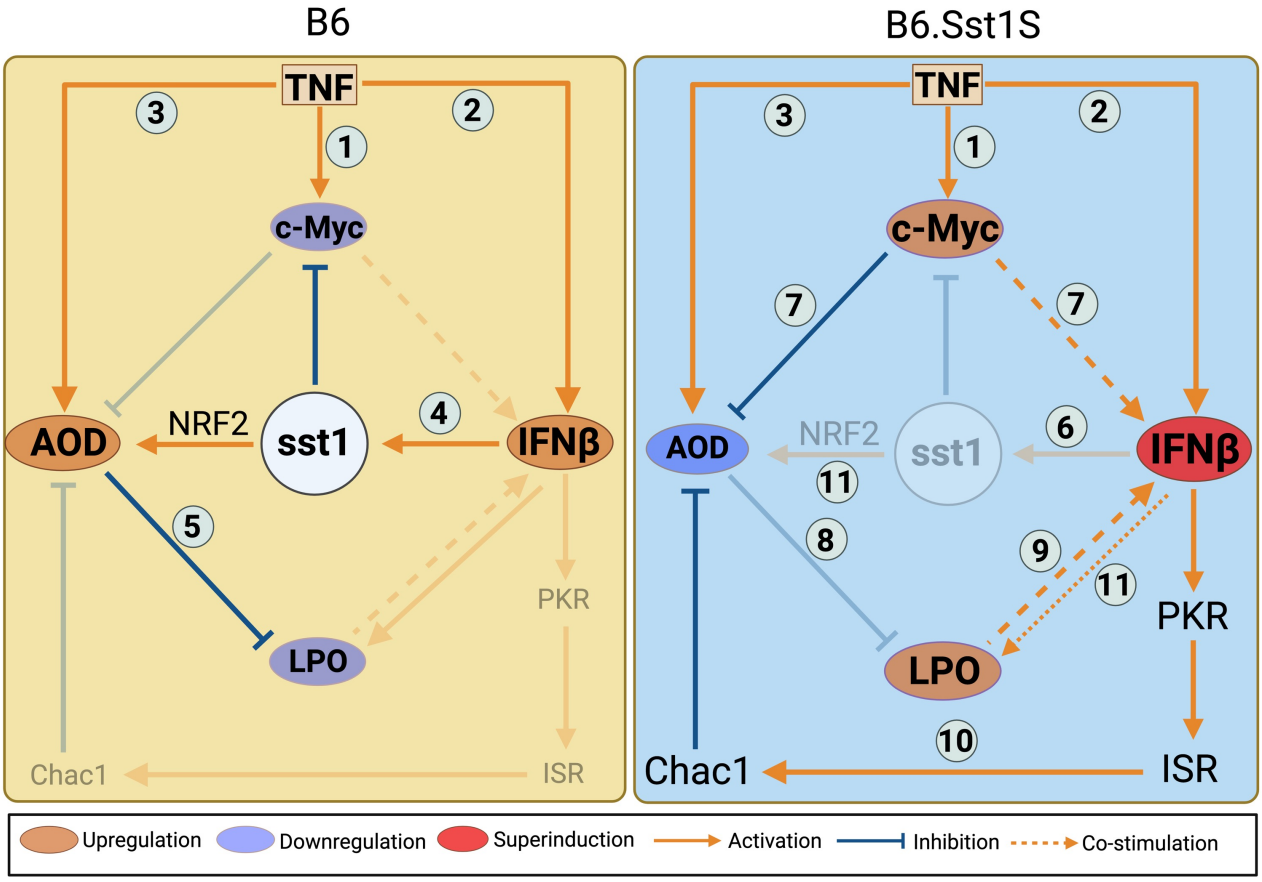
B6
B6.Sst1S
TNF
c-Myc
AOD
NRF2
sst1
IFNβ
LPO
PKR
Chac1
ISR
1
2
3
4
5
6
7
8
9
10
11
Upregulation
Downregulation
Superinduction
Activation
Inhibition
Co-stimulation

Figure 8